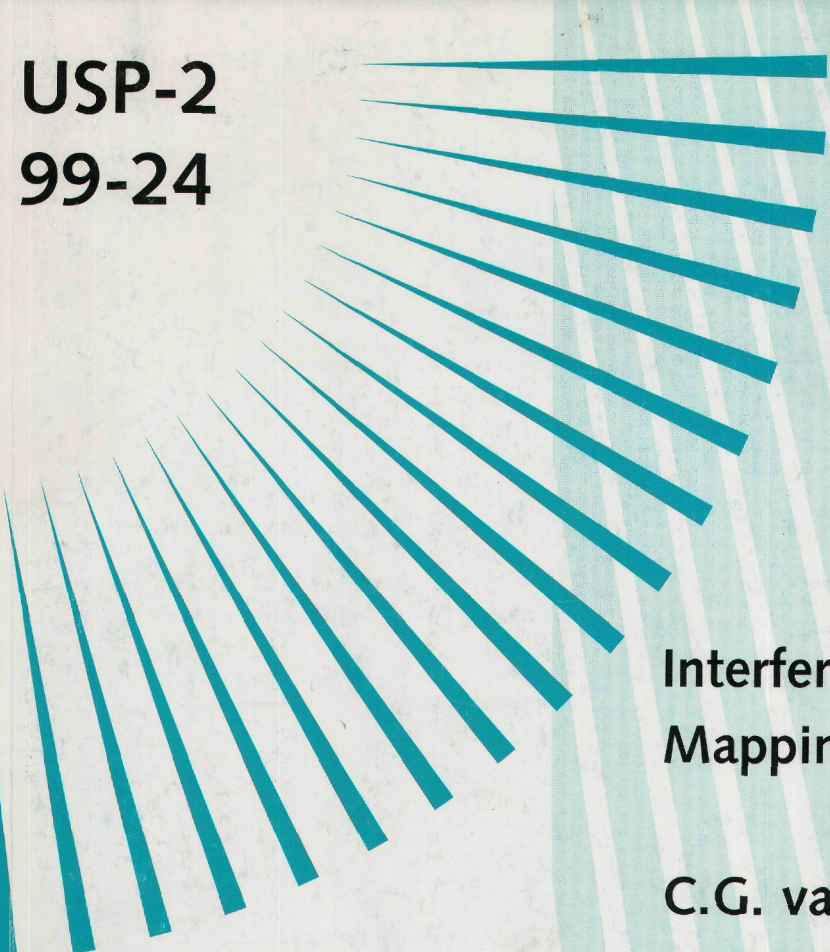


**USP-2
99-24**



**Interferometric Shoreline
Mapping**

C.G. van Koppen

J.S. Groot

J. Vogelzang

Y. Dierikx-Platschorre



USP-2 99-24



BELEIDSCOMMISSIE REMOTE SENSING

J. S. Groot

Interferometric Shoreline Mapping

C.G. van Koppen

ARGOSS

J.S. Groot

TNO-FEL

J. Vogelzang

K. Dierikx-Platschorre

Rijkswaterstaat-Survey Department

USP-2 report 99-24

USP-2 project 2.2/AP-04

ISBN 90 54 11 296 4

March 2000

This report describes a project carried out in the framework of the National User Support Programme (USP-2) under responsibility of the Netherlands Remote Sensing Board (BCRS) and the Space Research Organization Netherlands (SRON)

Abstract

Information on the location and evolution of shorelines is valuable. This information can be obtained from satellite Synthetic Aperture Radar (SAR) imagery. Direct, unsupervised classifications methods give poor results because of the high noise level in SAR images and the scattering properties of (wet) land and water. In this project is investigated how the phase information in Single Look Complex (SLC) SAR data can be used to give better results.

To obtain shoreline locations from SLC images a two-stage processing approach was developed. In the first stage phase information is used to obtain a reliable, robust land-water classification, though at the expense of the resolution. For this, interferometric methods (phase correlation) were used, but also algorithms that require only one SLC image were investigated.

In the second stage the accuracy of the position of the shoreline is improved using the full resolution of SLC images. The shoreline is represented as a spline to ensure smoothness. The coefficients of the spline are adjusted to maximise the intensity difference across the boundary, under the condition that the spline remains confined to the regions found in the first stage.

The developed algorithms were applied in a test area in the Waddenzee, a shallow sea north of the Netherlands. This area contains part of the main land, an island and numerous shoals that are periodically submerged. For validation of these results reference data were collected, such as laser altimeter measurements and tidal elevation model results. The shorelines obtained from SLC images showed a general agreement with the validation data. However, because of the flatness of the beaches in the area, even the best available reference data were not sufficiently accurate to validate the shorelines determined from SAR images.

Executive summary

In many countries, in particular in the developing world, adequate data on the shoreline and seabed are scarcely available. Satellite remote sensing offers, at least in principle, a worldwide source of such data. The project "Interferometric Shoreline Mapping" aimed at evaluating algorithms to extract land-water boundaries from ERS SAR (Synthetic Aperture Radar) images. The images used in this project cover a part of the "Waddenzee" bordering Groningen. This area was chosen to examine the possibility of extracting shorelines of regularly flooded sandbanks and of permanently dry land.

Various algorithms to detect a land-water boundary were investigated and are described in chapter 3. It describes seven different algorithms, which utilise the following quantities extracted from the SAR data:

- 1 power spectrum shift,
- 2 power spectrum width,
- 3 number of looks,
- 4 azimuth resolution,
- 5 multiple SAR looks,
- 6 coherence,
- 7 coherence combined with intensity.

Algorithms 6 and 7 use two ERS1/2 SLC images, the others only one. The algorithm involving azimuth resolution (4) is the only single image method investigated sensitive to land-sea differences. A limitation of the method is the use of a moving window, which smears land-sea boundaries. The method of creating separate images (looks) by filtering ERS images in the Doppler frequency domain (5) is on theoretical grounds shown to be of no use for the purpose of land-sea separation. Straightforward classification based on the coherence (6) yielded a visually good result. Inclusion of intensity (7) spoiled the result. The main conclusion is that classification based on coherence alone provides the best result as a first estimate.

The shorelines detected with the coherence algorithm are refined with the use of the full resolution intensity image containing the highest water level. The full resolution images can offer additional information to refine the contours. This refinement is only possible when the coherent areas coincide with structures visible in the intensity images within a certain bandwidth. The resulting shorelines were compared to shorelines obtained by intersecting water level and depth data (obtained from measurements and models). The agreement was poor. This is most probably due to the highly variable and shallow area in which the comparison was done. For example, sandbanks can change on small scale (ripples) due to the occurrence of high tide in between SAR passes. The coherence then disappears, although visually (on a larger scale), the sandbank's shoreline did not change. For a possible follow up experiment it is therefore recommended to use a test area with a well-defined shoreline, and to perform in situ observations of the coast during the SAR overpasses.

For dissemination of the research a WEB-version of this report can be found on:
www.argoss.nl:\ism\index.html

Contents

List of tables

List of figures

1	Introduction	1
1.1	Background.....	1
1.2	Objective.....	2
1.2.1	<i>Description of the technical approach adopted to tackle the problem</i>	2
2	Data	3
2.1	SAR Data.....	3
2.2	Tidal information at the time of image acquisition	3
2.2.1	<i>The Waddenzee model</i>	3
2.2.2	<i>Interpolation of the water level</i>	4
2.2.3	<i>Comparison with measurements</i>	4
3	Classification algorithms	5
3.1	Classification using a single SLC image	6
3.1.1	<i>Satellite SAR data processing parameters</i>	6
3.1.2	<i>Power spectrum shift</i>	7
3.1.3	<i>Power spectrum width</i>	7
3.1.4	<i>Number of looks</i>	8
3.1.5	<i>Azimuth resolution</i>	8
3.2	Classification using single pass, single antenna SAR interferometry	9
3.2.1	<i>The phase coherence of fore- and aft looks</i>	9
3.2.2	<i>Spatial decorrelation</i>	10
3.2.3	<i>Partial spectral overlap</i>	11
3.2.4	<i>“Super-Nyquist” SAR</i>	11
3.3	Classification using dual pass interferometry	12
3.3.1	<i>Classification using coherence</i>	12
3.3.2	<i>Combining coherence with intensities</i>	13
3.4	Conclusion.....	14
4	Coherence based Shoreline Detection	15
4.1	Simulated interferogram generation	15
4.2	Edge detection	16
4.3	Full resolution lines.....	17
4.4	Test lines.....	17
4.5	Conclusion.....	18
5	Coast line validation	18
5.1	Prospects of using other SAR sources.....	20
5.2	Cost-benefit analysis	20
5.2.1	<i>Governmental organisations in the Netherlands</i>	20
5.2.2	<i>Private sector; application in developing countries</i>	21
5.3	Conclusion.....	22
6	Conclusions	23

References

Figures

Appendices

List of tables

- 1 SAR images of the ISM database.
- 2 Stations in the eastern part of the Dutch Waddenzee where the water level is measured continuously. The co-ordinates are in the RDM system.
- 3 Measured and calculated water levels at the two stations in the area of interest for the recording times of the SAR images.

List of figures

- 1 Grid points of the Waddenzee model for the area of interest around Schiermonnikoog (blank area left of the centre).
- 2a Depth/Height map of the island of Schiermonnikoog and its surroundings.
- 2b Height map recorded with laser altimetry overlaid on ordinary 1:50000 topographic maps.
- 3 Interpolation of the water level at the coarse Waddenzee model grid (circles) to the fine grid of the depth map (plusses).
- 4 ERS-2 image (intensity) of orbit 5244 (left) and the coherence of the interferogram extracted from a tandem pair of ERS-1/ERS-2 (orbit 24917/5244) images.
- 5 Amplitude sum of ERS-2 data (left) and mean coherence (right).
- 6 Power spectrum (spectrum centroid \approx 126.6 if the frequency is 1,2,3...256).
- 7 Centroid position.
- 8 Spectrum widths.
- 9 Spectrum width image.
- 10 Number of looks, averaged over 10 lines.
- 11 Resolution estimate.
- 12 Line of ERS-2 data.
- 13 Normalised spectrum of the data of Figure 17.
- 14 Fore- (left) and aft looks (right).
- 15 Phase coherence.
- 16 Phase coherence for different overlaps (upper left= 0.2, upper right= 0.4, lower left= 0.6, lower right= 0.8).
- 17 Coherence computed from ERS-1/2 images (orbit 24917/5244; see Figure 18).
- 18 Coherence histogram corresponding to Figure 17.
- 19 Classification result of thresholding.
- 20 Result of Gaussian MAP classification.
- 21 Intensity of ERS-1/2 images (orbit 24917 (left)/5244 (right)).
- 22 Estimated coherence for simulated data (left) and theoretical result (right).
- 23 Profile across edge (left: single result; right 1000 results averaged).
- 24 Edge detected image.
- 25 Result of edge detection with the Sobel (left; PCI routine FSOBEL) and Prewitt (right; PCI routine FPPE) operators.
- 26 Result of edge detection with a 3 \times 3 differencing edge detection filter (PCI routine FED).
- 27 Coherence map of the island of Schiermonnikoog using the tandem pair ERS images of 20-21 April 1996.
- 28 Edge map of the island of Schiermonnikoog after removing solitaire edge points.
- 29 Result of the interpolation.
- 30 Enlargement of the interpolated edge at full resolution.
- 31 The original master image (left) and the image transformed to RD (right).
- 32a Coast line (red) overlaid on the land/water map.
- 32b Digital height map and tidal model grid points with the coast lines from the March pair (yellow), the April pair (red) and the shifted April coast line (blue).
- 32c April coastline and tidal model grid points.
- 32d Enlargement of Figure 32c including also the shifted April coastline (dark blue).
- 33 Land/water maps for April (left) and March (right).
- 34 Coastlines in red overlaid on the land/water map for the southern coast of Schiermonnikoog, the coast of the mainland, and the edge of a gully east of Schiermonnikoog (upper right).

List of figures (Continued)

- 35a The coherence map of ERS1/2 images (orbit 24416/4743 frame 2529) of March.
- 35b Intensity image of ERS 1 orbit 24416 frame 2529 (16 March 1996).
- 35c Intensity image of ERS 2 orbit 4743 frame 2529 (17 March 1996)
- 36 From upper left to lower right : noise f , impulse response function b , backscattering coefficients g and autoconvolution of g .
- 37 Land-water boundary detection using a cost function.

1 Introduction

1.1 Background

Information on shoreline position, shoreline evolution and seabed elevation is essential for planning of any developments at the coast, e.g. beach reconstruction, routing of pipelines and cables, mining of sand and minerals, hydrocarbon exploration, port and harbour development, and measures to protect the ecological and economic values of natural habitats. In many countries in particular in the developing world, adequate data on shoreline and seabed are rarely available. Satellite remote sensing offers a worldwide source of such data. Until now, data from satellites such as SPOT and Landsat have been used for this purpose, but with limited success due to the limited resolution, limited availability due to clouds, which is prohibitive for use in monitoring.

Two developments are likely to make satellite remote sensing a more valuable source of data for coastal mapping and monitoring. The first development is the increasing resolution, both spatial and spectral, of satellite borne optical sensors, that were launched recently or will be launched in the near future. The other development is the routine collection of SAR (Synthetic Aperture Radar) data, at present by ERS and Radarsat and in the near future by ENVISAT.

An existing application of satellite SAR imagery from ERS is the reduction of the cost of bathymetric surveys by combining a limited number of depth soundings with SAR imagery and a dedicated model of the interactions between seabed topography, currents, short waves and radar backscatter. This technique is now being embedded into bathymetric survey services both in the Netherlands and abroad. What has not been exploited sufficiently until now is the potential of SAR imagery for direct mapping of shorelines. This does not require in-situ data and can therefore be applied rapidly and at low cost to the monitoring of long stretches of coastline. The information is valuable in the planning stage of a project and for monitoring of change, e.g., to assess the effects of a building or reconstruction project.

Detecting shorelines from the standard multi-look SAR image product from ERS has not been entirely successful in the past. The NRSP study 2.2/TO-02 concluded that land-sea separation is difficult because the radar backscatter from shoals above the waterline is highly variable, due to variations in surface moisture content. Another disturbing factor is the wind, which modulates the land-sea contrast, and can even invert it. However, it is expected to be possible to improve the skill of separating land and sea surface by using phase information present in single-look complex imagery, which is routinely made available by ESA on request. The coherence between two complex images is always very low over sea (since the surface features change continuously) and considerably larger over land. We expect that an interferometric approach which combines phase information and backscatter intensity from multi-temporal single-look complex SAR imagery with tidal information, can be used successfully for shoreline mapping, and possibly for obtaining additional information about bed slope. Available models predicting the radar cross-section of the sea-surface and its variability (CMOD4, cut-off detection) may be useful as well for constraining the solution.

1.2 Objective

Our objective is to build this idea into a method for shoreline mapping from multi-temporal complex SAR imagery which is reliable enough for routine application world-wide. This method should offer

An optimal trade-off between resolution and accuracy (single-look imagery has the maximum attainable resolution and averaging of intermediate products can be done at the appropriate level in a manner most suitable for the problem).

Performance (using all discriminating surface properties including surface shape variability).

Reliability (all-weather performance of SAR and regular sampling).

1.2.1 Description of the technical approach adopted to tackle the problem

The development of an algorithm for determining shorelines from multi-temporal single-look complex SAR imagery was split up in three subtasks:

Preparation of data sets.

Detailed analysis of SAR data set.

Formulation and testing of algorithms for shoreline mapping.

The technical content of the work is described (as originally formulated) in more detail below:

1 Preparation of data-sets

Since 1992, TNO-FEL has collected single-look complex images from ERS over the eastern part of the Waddenze. This data set is very suitable for the proposed research. In order to keep the total volume of the data limited, a region will be selected to focus the present study on, the selection being dependent on lengths and types of coastlines present and availability of reference survey data (field surveys, laser altimeter data). For the selected region, compilation of suitable imagery, co-locating and geo-referencing of the images will generate a database of single-look complex SAR images.

2 Detailed analysis of SAR data-set

Start of the analysis is systematic mapping of single-image characteristics such as backscatter intensity and multi-temporal image characteristics such as coherence and backscatter variation in a test area. The results are related to reference in-situ data and to tidal phase. Initially, most attention is given to image characteristics for land permanently above the waterline and for the permanently submerged zone, after which the intertidal zone is studied in some more detail. Purpose is to test and possibly modify hypotheses about local image characteristics over water and land, and use the results to define an approach to extract shoreline position from single-look complex SAR imagery. The data-analysis will be guided by results from previous studies and models of radar backscatter over water and different types of land surfaces. Effects of processing parameters on the result of the analyses will be investigated.

3 Algorithm development and testing

The first step in the development of algorithms is to develop rules for discrimination based on several images and a single variable, such as coherence. The second step is to develop multivariate rules for discrimination. The third step is to test the resulting algorithm on a data set consisting of sub-scenes not used in the previous stages. RWS-MD will bring in geodetic expertise in comparing the results with several other data sets.

2 Data

This chapter describes the data set created by TNO-FEL. The tidal conditions at the acquisition time of the SAR images in the database are outlined in the second section of this chapter.

2.1 SAR Data

TNO-FEL has a database of SLC-images of the province of Groningen. From this database several images were processed in relation to this project. A strip of approximately 50-km x 20-km surrounding the island of Schiermonnikoog and the Lauwerszee is processed. The database created in the scope of the Interferometric Shoreline Mapping project contains 5 SAR images recorded around 10.30h GMT, see Table 1.

Date	Satellite	Orbit	Frame	Master/Slave
11-02-1996	ERS-2	4242	2529	S
16-03-1996	ERS-1	24416	2529	S
17-03-1996	ERS-2	4743	2529	S
20-04-1996	ERS-1	24917	2529	S
21-04-1996	ERS-2	5244	2529	M

Table 1 SAR images of the ISM database.

These images were prepared in order to fit the raster of the master image (ERS 2, orbit 5244). The accuracy of the co-registration of the images is better than 0.1 pixels. The slave images were corrected for the 'flat earth' phase pattern. This phase pattern is a result of slightly different view angles of the images. With the removal of the 'flat earth' it is possible to use an arbitrary pair of images from the ISM database to produce an interferogram.

2.2 Tidal information at the time of image acquisition

2.2.1 The Waddenzee model

The Waddenzee model calculates current velocity and water elevation by solving the shallow water equations within the well-known WAQUA system. The model is two-dimensional in the horizontal plane, so it yields depth-averaged currents. The effect of wind is included, but that of atmospheric pressure is neglected. The Waddenzee model receives its boundary conditions from similar models on a larger scale. The model employs a curvilinear grid. Figure 1 shows the grid points for the area of interest.

Water level fields were generated for the times the ERS SAR images were recorded. As can be inferred from Figure 1, the calculated water levels are on a grid that is much coarser than that of the SAR images and the maps of land and water derived from them. However, under the assumption that the water level varies smoothly over the area, a reliable interpolated field on a fine grid can be obtained. If also depth is known on a fine grid, a detailed land/water map can be constructed.

A detailed depth map on a 20 m × 20 m grid is available. It is based on the interpolation of echo soundings, see Figure 2. The accuracy of this depth map is not well known. It is estimated to be of the order of 20 cm, though this may be optimistic. For the isle of Schiermonnikoog a digital height map is available. This map is shown in Figure 2b, overlaid on an ordinary topographic map. The map is recorded with laser altimetry, and its accuracy is 15 cm. The 0-m level coincides with the transition from blue to dark blue. Note that the coastline on the topographic map is not entirely consistent with the 0-m level on the height map, like in the upper left part. Fusion of the depth map and the height map into one digital elevation map (DEM) of the test area has not been attempted since this is considered to be outside the scope of this project.

2.2.2 Interpolation of the water level

As shown in Figure 1, the grid of the Waddenzee model is curvilinear. Standard methods of interpolation, requiring regularly spaced support points, are therefore not applicable. Instead, the following procedure has been adopted (see Figure 3):

Starting from the points on the depth map (on a 10 m × 10 m grid), e.g., point *P*, the nearest water level support point, e.g., point *O*, is found. If point *O* coincides with point *P* (which actually happens for a few points), the water level at *P* is that at *O*.

The four nearest neighbours of point *O* are checked to select points *A* and *B* such that the vector *OP* lies between *OA* and *OB*. If one of the points *A* or *B* is missing because point *O* lies on the land/water boundary, the water level at *P* is taken the same as at *O*.

If *A* and *B* exist, the three-dimensional vectors *OA* and *OB* are calculated, with the z-components equal to the water level relative to that at *O*. The vector equation $\mathbf{n} \cdot \mathbf{r} = 0$, with $\mathbf{n} = \mathbf{OA} \times \mathbf{OB}$, defines the water level plane through the points *O*, *A*, and *B*. The water level at *P* is now readily obtained by substituting the horizontal co-ordinates of *P* relative to *O* in $\mathbf{n} \cdot \mathbf{r} = 0$ and solving for the z-component.

It happens for some points on the fine grid that point *P* lies just outside the triangle *OAB*. In those cases the water level is extrapolated over a small distance. Note that the use of the vector product in step 3 for defining the interpolating plane leads to a stable algorithm.

2.2.3 Comparison with measurements

At some locations in the Waddenzee, the water level is measured continuously by Rijkswaterstaat. The stations in the eastern part of the Waddenzee are listed in Table 2.

Station name	X (km)	Y (km)
Schiermonnikoog	209.170	609.500
Lauwersoog	208.850	602.790
Huibertsgat	221.990	621.330
Eemshaven	250.750	607.900
Delfzijl	258.000	594.430
Nieuw Statenzijl	276.540	584.310

Table 2 Stations in the eastern part of the Dutch Waddenzee where the water level is measured continuously. The co-ordinates are in the RDM system.

Comparison with Figure 2 shows that the stations “Eemshaven”, “Delfzijl”, and “Nieuw Statenzijl” are located east of the area of interest. Station “Huibertsgat” is just beyond the edge of the area of interest, and only stations “Schiermonnikoog” and “Lauwersoog” fall within the area. Table 3 shows the measured water levels at these two stations and the interpolated water levels at the most nearby fine grid point (which is at 22.4 m for station “Schiermonnikoog” and at 374 m for “Lauwersoog”). The water level is given in meters with respect to NAP, the time in GMT. The measured water levels in Table 3 are averaged over the 10 minutes period between 10:25 GMT and 10:35 GMT.

Date	Time	Station Schiermonnikoog			Station Lauwersoog		
		Measured	Calculated	Difference	Measured	Calculated	Difference
11-02-1996	10:30	+0.16	+0.06	+0.10	+0.16	+0.16	0.00
16-03-1996	10:30	-1.25	-0.86	-0.39	-1.24	-1.09	-0.15
17-03-1996	10:30	-0.49	-0.28	-0.21	-0.61	-0.46	-0.15
20-04-1996	10:30	+1.05	+0.98	+0.07	+1.04	+1.01	+0.03
21-04-1996	10:30	+1.00	+0.91	+0.09	+0.99	+0.94	+0.05

Table 3 Measured and calculated water levels at the two stations in the area of interest for the recording times of the SAR images.

The difference between measured and calculated water level is generally small, except for 16-03 and 17-03. Both stations give considerable deviations for these two consecutive days, probably due to some effect not included in the models. For the other days the deviations are within 10 cm at “Schiermonnikoog” and within 5 cm at “Lauwersoog”. It is therefore assumed that the interpolated water level has an error of about 10 cm, except for 16-03 and 17-03.

3 Classification algorithms

The problem of detecting the sea-land interface (shoreline) is generally called an edge detection problem. An edge is characterised by a jump in (average) grey level. Edge detection is for example treated in [Pratt, 1978]. Detecting (which includes locating) an edge in an interferometric coherence image is difficult because of the noisy character of the data. Furthermore, the measured coherence is only an approximation of the real coherence, which causes additional problems. In the following we will show a method that detects edges with considerable precision in a simulated interferogram, and also apply it to ERS interferometric tandem data.

This chapter describes six different methods that were investigated for their capability of extracting the land-water boundary from the SAR images. They use:

power spectrum shift,
power spectrum width,

- 1 number of looks,
- 2 azimuth resolution,
- 3 multiple SAR looks from single SAR system,
- 4 coherence,
- 5 coherence combined with intensity.

Except for the last two methods all methods use a single ERS1/2 SLC image.

3.1 Classification using a single SLC image

The test data used was a rectangular patch of SLC ERS-2 data (orbit 5244) consisting of 10 lines (parallel to the flight track) of 7000 pixels, covering both land and sea. The patch is indicated by the vertical white bar at the bottom of the left image of Figure 4. For comparison we included a coherence image of the same area at the right. It is clear that the boundary between land and sea is sharper defined by the coherence image than by the intensity image. This is also obvious from Figure 5. At the left is a plot of the sum of the amplitudes of the 10 lines (left-right corresponds to top-bottom in Figure 4). The higher values correspond to land, the lower ones to sea. The rectangles at the bottom indicate the presence of land. The four rectangles are (from left to right): Schiermonnikoog, a bridge/dike, a protruding piece of land ("De Dijk") and the main land (Groningen). The boundaries were simply determined by thresholding at value 200, and omitting too small land areas. At the right is a plot of the (10 line) average coherence. The boundaries are much sharper in this case. In this note we will only use the complex data of the ERS-2 image.

3.1.1 Satellite SAR data processing parameters

Processing of satellite SAR data is usually done by correlating the raw data with range and azimuth reference functions. The azimuth reference function is based on the phase history of a stationary point target. The associated Doppler frequency history is [de Vries, 1991]

$$f(t) = f_{DC} + f_{DR}t,$$

with

f	[Hz]	Doppler frequency,
t	[s]	time elapsed since the point target passed the antenna foresight direction,
f_{DC}	[Hz]	Doppler centroid,
f_{DR}	[Hz/s]	Doppler (frequency) rate.

Generally, when incorrect values for the Doppler centroid and/or Doppler rate are used the image quality degrades both radiometrically and geometrically. Because the centroid and rate are based on the assumption of a stationary target, it is to be expected that the image data of moving targets (like the sea) differ from that of non-moving targets (e.g., land).

3.1.2 Power spectrum shift

Processing data of stationary targets with a wrong Doppler centroid results in a shift in the azimuth direction proportional to the difference between the right and wrong Doppler centroid. This is also visible as a frequency shift in the power spectrum of the complex image data. Because moving targets are always processed with a wrong Doppler centroid, their spectrum will be displaced. So if the sea moves (sufficiently fast in one net direction), its image spectrum will be shifted compared to that over land. We used the following algorithm to compute the “centroid” of our data:

```
1 for line 1 to 10
2   for each 256 pixel segment of the line
3     compute power spectrum  $|\text{FFT}(256 \text{ complex samples})|^2$ 
4     compute spectrum centroid (the power sum left of the centroid equals that to the right)
5   end
6 average centroids of 10 lines
7 end
```

Figure 6 shows an example of the output of step 3. Figure 7 shows the final outcome of the algorithm.

The rectangles at the bottom of the graph indicate the presence of land as in Figure 5. There is no correlation between the occurrence of land and the centroid position. This could be caused by a negligible water surface velocity (due to the absence of wind).

3.1.3 Power spectrum width

Although no shift of the spectrum was found, a broadening could be present. Therefore we computed (similarly to the above algorithm) average spectrum widths along 10 lines, and averaged the results. For a single spectrum the width is defined by

$$w = \sum_{i=1}^{256} p(i)|i - c|,$$

with i proportional to the frequency, p the normalised power spectrum ($\sum_{i=1}^{256} p(i) = 1$) and c the

centroid position determined above. Figure 8 shows the widths. In this case there is a link between the width and the occurrence of land: the width is larger above sea. Figure 9 shows the widths computed for the entire image. Comparing this image to Figure 4 reveals that the spectrum width does not really distinguish land from water, but rather high (land and wind streaks on the water) from low backscatter intensity (calm water) regions. We do not yet have an explanation for this effect.

3.1.4 Number of looks

The Doppler rate f_{DR} can be computed from ancillary data (i.e., spacecraft flight data) or from the SAR data itself. The latter method is called “autofocus”. A test of an autofocus algorithm detailed in [de Vries, 1991] revealed that the algorithm did not function properly above sea. The reason was the lack of relatively bright targets over sea, compared to land. A measure for this lack is the number of looks of the data: if there are no point targets the (backscattering coefficient) data will be exponentially distributed, with the number of looks equal to

$$N = \sqrt{\frac{m}{\sigma}},$$

with m the mean of the data and σ the standard deviation. If there are point targets present the number of looks will most often be smaller. Figure 10 shows the number of looks computed for our test data. The values were computed over 100 pixel line segments. There is only in some cases a correlation between the occurrence of land and a relatively small number of looks (especially near pixel 5000). The number of looks is therefore of no use.

3.1.5 Azimuth resolution

SAR processing assumes a stationary scene. Intuitively one expects the spatial resolution (in azimuth) of more or less randomly moving parts (like the sea) to be possibly worse than that of non-moving parts. Because no bright point targets are present at sea, it is impossible to measure this resolution directly. However, the resolution can be estimated from the (speckled) data of a homogeneous surface [MAST C-STAR project group, 1998]. In the Appendix it is proven that, under certain assumptions, a resolution estimate is

$$\rho_a = \frac{w\left(F^{-1}\left(|F(g)|^2\right)\right)}{\sqrt{2}},$$

with

- ρ_a azimuth resolution [m],
- w a function returning the 3 dB width of its argument (a peaked function) [m],
- $F^{(-1)}$ (inverse) Fourier transform,
- g a line segment of backscattering coefficients (σ^0) with mean 0.

We computed this resolution estimate for our test data. Because g is a real function with 4 m sampling distance and 5.4 m resolution (determined from corner reflector signatures) we interpolated the complex SLC data by a factor 2 first. To get a better estimate for ρ_a we averaged the power spectra $|F(g)|^2$ of 10 adjacent line segments. The result is shown in Figure 11.

The smallest resolution (5.4 m) occurs above sea. This value happens to be equal to the one derived from corner reflector signatures. The resolution is consistently higher over land than over sea. The Appendix provides a probable cause for this effect. Apparently this effect is more important than any resolution spoiling effect due to sea surface movement (in this case).

3.2 Classification using single pass, single antenna SAR interferometry

In interferometry two complex SAR images are combined to form an interferogram, containing phase information. A prerequisite for a useful interferogram is a certain degree of phase coherency between the two images, defined as

$$\rho = \frac{|E(b_1 \circ b_2^*)|}{\sqrt{E(b_1 \circ b_1^*)E(b_2 \circ b_2^*)}}$$

b_1 and b_2 are complex matrices holding the complex pixels of image 1 and 2, respectively. E stands for the statistical expectation operator (operating over a sub-image), \circ for elementwise multiplication and $*$ for complex conjugation. The coherency can change due to changes in the scene between the datatakes (temporal decorrelation), or due to a difference in aspect angle between the two datatakes (e.g., baseline decorrelation), amongst others.

A single look complex SAR image can be used to create two images (looks) with half the original resolution by SAR processing the negative and positive Doppler frequency data separately. This gives a backward (“aft”) and forward (“fore”) look, respectively. The small time and azimuth angle difference between the two looks suggests that the interferogram formed by the two looks contains useful information, especially for the purpose of distinguishing (slowly decorrelating) land from (fast decorrelating) sea. This is only possible if the sea surface decorrelates in the time interval between the two looks. The maximum of this time interval is estimated as follows: the ERS (10 m length) antenna’s two-way 3 dB beamwidth is approximately 0.21° [Attema, 1991]. The footprint due to this beamwidth is 3.1 km. The beam traverses this footprint in 0.5 sec.. The time interval between the two looks is therefore at most 0.5 sec. The decorrelation of a water surface takes place in two steps: a steep decrease in correlation after ≈ 10 ms (due to the short waves), followed by a slower decorrelation after ≈ 0.5 -1 s (due to the longer waves). Due to the first step the water surface decorrelates at least partly in the time between the two looks, so this is no problem.

In the following we will experimentally show that no correlation exists between the fore- and aft look, and prove theoretically why.

3.2.1 The phase coherence of fore- and aft looks

Fore- and aft looks are created from the complex image in three steps:

Perform a Fast Fourier Transform (FFT) on a line (parallel to the flight track) of n (even) complex pixelvalues.

Split the result in two halves of length $n/2$, corresponding to negative and positive frequencies (taking a possible Doppler offset into account).

Perform an Inverse Fast Fourier Transform (IFFT) on the two halves (padded with zeros to length n) separately. This gives the fore- and aft-looks. An example: Figure 12 shows the absolute values of 7000 pixels of ERS-2 data obtained over “de Waddenzee” in the Netherlands. The higher values correspond to land, the lower ones to sea. Figure 13 shows the spectrum of this line. The spectrum was shifted such that zero frequency appears at the centre.

The aft look was created by putting zeros at the positive frequencies in the spectrum, the fore look by putting zeros at negative frequencies. After IFFT'ing these two spectrum halves separately the fore- and aft looks of Figure 14 result. Finally, Figure 15 shows the phase coherence between the fore- and aft looks (the coherence was estimated by averaging over 50 pixels). The coherence is small, and, even more important, the coherence above land does not differ from that above sea.

The intuitive notion of the existence of some degree of coherence between the fore- and aft looks (at least above land) is most probably wrong. In the following the cause of the absence of any coherence is investigated.

3.2.2 Spatial decorrelation

If the look directions (in azimuth) of two satellite passes differ by more than a certain angle α total decorrelation of the two images results. [Gabriel and Goldstein, 1988] and [Zebker and Villasenor, 1992] give for this angle

$$\alpha = \frac{\lambda}{2\rho_a},$$

with λ the wavelength [m] and ρ_a the azimuth resolution [m] of the images. This relation assumes uncorrelated scattering centres within the beam and a sinc-like system impulse response. A single look ERS image has an azimuth resolution of 5.4 m. The fore- and aft looks are created by using half of the Doppler spectrum and thus have twice this resolution. Therefore, $\alpha \approx 0.15^\circ$ for the ERS.

If the corresponding angle α' between the fore- and aft look exceeds (equals) this angle, no (little) correlation will exist between the fore- and aft look. This angle is derived as follows: assume a radar with synthetic aperture length L [m] flies by a point target. When the point target enters the beam the radar records positive Doppler frequencies, decreasing to 0 when the target is halfway the aperture, after which the Doppler frequencies become more and more negative. The fore- and aft image of the point target are computed from the positive and negative frequency data, respectively (i.e., from completely different data, suggesting non-coherence). The separation between fore- and aft look is then approximately $L/2$, which gives

$$\alpha' = \frac{L}{2R} = \frac{\lambda}{4\rho_a},$$

with R the radar-target distance [m]. We used the following expression for the SAR resolution:

$$\rho_a = \frac{\lambda R}{2L}.$$

For the ERS $\alpha' \approx 0.15^\circ$ (this time we have to use $\rho_a = 5.4$ m), which equals α .

This explains why no coherence is present in Figure 15: the fore- and aft looks are independent because the look directions differ too much. It is easily shown that this not only holds for 2 (fore- and aft) looks, but for each number of looks (e.g., 3 by dividing the spectrum in 3 parts).

3.2.3 Partial spectral overlap

Instead of splitting the spectrum of Figure 13 in two distinct halves it is possible to use overlapping halves. In this way the resolution of the resulting fore- and aft looks stays the same (and therefore α , too), but the fore-aft look difference α' decreases. This suggests an increase of coherency with overlap. Figure 16 shows the coherence for increasing overlaps (e.g., if the overlap is 0.2 the spectra have $0.2 \times 3500 = 700$ values in common; the common part is centred round zero frequency). The coherence increases with increasing overlap, but no difference between sea and land shows up (e.g., a faster increase of the coherence above land than above sea). The reason is simple: the increasing overlap of the spectra causes the overall increasing coherence, while the non-overlapping parts stay at a distance of $L/2$ (i.e., the fore-aft look difference α' for these parts stays the same), resulting in non-coherence between these parts. Similar results are obtained for the amplitude coherence (i.e., by using the amplitude instead of the complex images), although the average coherence is much higher.

3.2.4 "Super-Nyquist" SAR

[Fitch, 1990] describes a single antenna interferometer and shows as result an interferometric fringe above the ocean, probably caused by a ship induced internal wave. The procedure is simple:

- a) Obtain SAR data at a ("super-Nyquist") PRF twice that needed according to the Nyquist criteria (this latter frequency is $PRF = 2v/l$, with v the platform velocity [m/s] and l the antenna length [m]. In practice a (5-10 %) higher PRF is used to suppress sidelobes).
- b) Split the data set in two halves (containing the odd and even pulses).
- c) SAR processes the odd and even data sets into images with resolution $l/2$ (this is possible because both the odd and even data sets consist of samples taken at the Nyquist frequency).
- d) Interpolate the odd image by half a pixel distance to let it coincide with the other image (this is equivalent to squinting it).
- e) Compute an interferogram with the two images.

Using a "super-Nyquist" PRF in a) might seem useless, because conventional SAR theory uses the fact that the Doppler signal should only be sampled at its Nyquist frequency (not higher). However, this only holds for time-independent targets (like land). For time-dependent targets (like sea) it probably pays off to use a higher PRF.

Step d) creates an image with a look angle (in azimuth) slightly different from that of the even image. The difference is

$$\alpha' = \frac{l}{4R},$$

with R the ground range distance from radar to target. As in the preceding discussion α' should be smaller than α to measure any coherence at all, which leads to

$$\frac{l}{4R} < \frac{\lambda}{2\rho_a} \Rightarrow R > \frac{l^2}{4\lambda}.$$

For the PHARUS system this is obviously no restriction. Whether this result can be generalised (i.e., whether it is useful to squint the odd image by more than half a pixel) like [Fitch, 1991] suggests is questionable.

The time interval between the two images is

$$\Delta t = \frac{l}{4v},$$

which is about ($l=1$ m, $v=100$ m/s) 2.5 ms for PHARUS. This is smaller than the decorrelation time of the sea, but possibly long enough to observe a sufficient coherence difference between land and sea. A favourable condition is a small flying speed

The PHARUS is also well suited for this technique, because it can sample PRF's of up to a few kHz, while the Nyquist PRF is typically 200 Hz. The above method is not applicable to ERS imagery, because the PRF (1640-1720 Hz) is only slightly higher than the Nyquist criteria (ground speed 7.7 km/s and antenna length 10 m demand a PRF of 1540 Hz).

3.3 Classification using dual pass interferometry

3.3.1 Classification using coherence

Inspection of the coherence image of a tandem pair of ERS images suggests that the coherence enables one to distinguish between land and sea (see Figure 17). This is to be expected: the (real) coherence of sea is 0, while that of land will mostly be larger than that. This is quantified by Figure 18, showing a histogram of the coherence of Figure 17.

The histogram exhibits two peaks. The left one is due to the water (maximum at coherence 0.15, average coherence 0.17), the right one to land (maximum at 0.75, average 0.72). About 86 % (14 %) of the image belongs to the left (right) peak. The average coherence of the water is related to the number of pixels averaged. [Oliver and Quegan, 1998; p. 346] give

$$\langle \rho \rangle \approx \sqrt{\frac{\pi}{4n}},$$

with

- $\langle \rho \rangle$ average measured coherence if the real coherence is 0 (as for sea),
- n number of pixels averaged for the coherence computation.

In our case one expects $\langle \rho \rangle \approx \sqrt{\pi/(4 \times 45)} \approx 0.13$. Our measurement 0.17 (corresponding to $n \approx 27$) is slightly higher. This could be due to a residual dependence between the pixels averaged.

A simple thresholding operation with a suitable threshold results in the classification result of Figure 19. The threshold was chosen such that just a few white speckles (land pixels) started to appear in the sea part of the image.

3.3.2 Combining coherence with intensities

Although the result is satisfying, it is interesting to test whether combining the coherence and intensities of two repeat pass ERS images improves the classification result of this figure. [Oliver and Quegan; pp. 427-430] provides a general method for this, called Gaussian MAP (Maximum A Posteriori) classification. The method uses the following four steps:

- 1 Compute the determinant of C_n (the covariance matrix) for both a land and sea training area:

$$|C_n| = \sigma_{1n}\sigma_{2n}(1 - |\rho_n|^2),$$

with

- n class (1= land, 2= sea),
- ρ_n coherence for land or sea training area,
- σ_{1n} backscattering coefficient of land or sea training area in first ERS image,
- σ_{2n} backscattering coefficient of land or sea training area in second ERS image.

- 2 Compute the covariance matrix for each area to classify (test area):

$$A = \begin{pmatrix} \sigma_1 & \sqrt{\sigma_1 \sigma_2} \rho \\ \sqrt{\sigma_1 \sigma_2} \rho^* & \sigma_2 \end{pmatrix},$$

with

- ρ coherence of the test area,
- σ_1 backscattering coefficient of the test area in the first ERS image,
- σ_2 backscattering coefficient of the test area in the second ERS image.

- 3 Compute the trace ('tr') of $C_n^{-1}A$ (also for each test area, and for $n=1,2$):

$$\text{tr}(C_n^{-1}A) = \frac{1}{1 - |\rho|^2} \left(\frac{\sigma_1}{\sigma_{1n}} + \frac{\sigma_2}{\sigma_{2n}} - 2 \sqrt{\frac{\sigma_1 \sigma_2}{\sigma_{1n} \sigma_{2n}}} \text{Re}(\rho \rho_n^*) \right)$$

'Re' returns the real part of its complex argument.

- 4 Finally, compute d_n for each test area and for $n=1,2$:

$$d_n = -\ln P(n) + L \left(\text{tr}(C_n^{-1}A) + \ln |C_n| \right),$$

with

- L number of looks of the image (45 in this case)
- $P(n)$ a priori probabilities ($P(1)=0.15$, $P(2)=0.85$ in this case).

The area is classified as land if $d_1 < d_2$ and as sea otherwise.

Step 1 is performed once at the beginning of the classification procedure of an entire image, while steps 2-4 have to be repeated for each area to be classified. Figure 20 shows the result of this classification for the same images as of Figure 4. The grey value is proportional to d_1/d_2 , so that dark (light) areas are classified as land (sea). The result is obviously worse than that of Figure 19. Figure 21 shows why.

The ERS-1 image shows little contrast between land sea, while the ERS-2 image exhibits light streaks north of land parts. These phenomena show up in the classified image because the algorithm is not able to decide which information is more valuable: that of the coherence or of the intensity images. Obviously, the information content of the coherence image is superior.

A peculiarity of the classification procedure is the use of $\text{Re}(\rho\rho_n^*)$ in step 3. This quantity is proportional to $\cos(\angle\rho - \angle\rho_n)$. Generally, the phase becomes less well defined the smaller the coherence. The sea is a limiting case: the coherence is zero, so the phase is completely undetermined. Moreover, any residue of incorrect phase unwrapping (e.g., omission of the flat earth correction) influences the classification through the aforementioned quantity. The classification depends therefore partially on a more or less undefined quantity. A solution is to replace it by an expression with roughly the same behaviour (with respect to the range, the value when ρ is near ρ_n , etc.), but without any unwanted phase dependence. We tried

$$\left(1 - 2\left|\left|\rho\right| - \left|\rho_n\right|\right|\right)\left|\rho\rho_n\right|$$

The classification result differed only marginally from Figure 20. So this change is unimportant.

3.4 Conclusion

The method involving azimuth resolution (Figure 11) is the only single image method investigated sensitive to land-sea differences. A limitation of the method is the use of a moving window, which smears land-sea boundaries. Another disadvantage is that classification needs a threshold unknown in advance. The method performs most probably worse than interferometric (two image) methods.

The method of creating separate images by filtering ERS images in the Doppler frequency domain is of no use for the purpose of land-sea separation. Apparently the SAR processing already “uses all coherence available from the raw data”, leaving none for our application. On the other hand, a SAR operating at a PRF of twice the Nyquist rate (or higher) is able to measure two (or more) images of the same surface, effectively obtained at slightly different times. Due to the sea decorrelation these images will show some decorrelation. It would be interesting to obtain PHARUS data at a “super-Nyquist” rate of some land and sea to test this technique.

Straightforward classification based on the coherence yielded a visually good result. Inclusion of intensities spoiled the result. The main conclusion of this chapter is that classification based on coherence alone provides the best result. This method is examined in more detail in the next chapter.

4 Coherence based Shoreline Detection

The generation of a shoreline using the coherence classification method is outlined in this chapter. First the line detection algorithm is explained and then tested quantitatively on synthetic data, and tested qualitatively on real data. It is then applied to a limited test area.

4.1 Simulated interferogram generation

An interferogram is computed by multiplying a complex SAR image by a precisely co-registered complex conjugated SAR image, and averaging the result (over 3 range times 15 azimuth pixels in our case). A good quality interferogram results only if the two SAR images are correlated. A synthetic interferogram can therefore be computed from two simulated correlated SAR images.

Correlated data sequences can be generated by filtering. The following simple algorithm serves as an illustration:

- 1 Generate a vector $x(i)$ ($i= 1, 2, \dots, 2n$; n an integer >1), with x drawn from a uniform random distribution $[-0.5, 0.5]$.
- 2 Filter x as follows: $y(i)= ax(i)-bx(i-1)$ ($i= 1, 2, \dots, 2n$), with a and b real numbers.
- 3 Generate $c(i)= y(2i-1)$ ($i= 1, 2, \dots, n$) and $d(i)= y(2i)$ ($i= 1, 2, \dots, n$).

Step 2 relates the odd (c) and even (d) neighbouring elements of y to each other, which results in a non-zero coherence between c and d . It is easily shown that this coherence is

$$\rho \equiv \frac{\left| \sum_{i=1}^n c(i)d(i) \right|}{\sqrt{\sum_{i=1}^n c^2(i) \sum_{i=1}^n d^2(i)}} = \frac{ab}{a^2 + b^2},$$

for n sufficiently large.

A more complicated algorithm [Fernandes, 1998; P.A. Kelly *et al.*, 1988], still based on the above filtering idea, computes two complex SAR images A and B with the following characteristics (input by the user):

- l number of lines of A and B (integer),
- p number of pixels of A and B (integer).
- σ Standard deviation of the Gaussian distributed real/complex part of both images (real).
The average of the squared absolute elements of A and B is $2\sigma^2$ (= backscattering coefficient).
- ρ_h correlation between horizontally adjacent pixels (complex),
- ρ_v correlation between vertically adjacent pixels (complex),
- ρ coherence between images (complex).

To verify the algorithm we computed the coherence for images simulated with $l=50, p=50, \sigma=1, \rho_h=0.2+0.2i$ and $\rho_r=0, 0.1, \dots, 0.8$. The coherence was computed for numbers of pixels ranging from 2 to 1600, with as result Figure 22 (left). The 9 decreasing curves in the figure correspond to the 9 coherences 0, 0.1, ..., and 0.8. The computed coherences converge to the real ones at the right of the figure. On average the computed coherence always exceeds the real coherence. For comparison the theoretical result [Oliver and Quegan, 1998] is shown at the right. The curve for coherence 0 obeys the simple equation

$$\rho = \sqrt{\frac{\pi}{4n}}$$

with ρ the coherence and $n (> 10)$ the number of looks. The good correspondence between the simulated and theoretical results illustrates the validity of the simulation method.

4.2 Edge detection

For the investigation of a good edge detection algorithm based on a step in coherence, we generated two images with the algorithm outlined in the previous section. The left of the images (up to and including pixel 40) had coherence 0.8 (which is typical for ERS tandem images of land), the right half 0 (because sea decorrelates completely within a few milliseconds). The exact intersection is therefore located at 'pixel' 40.5. We then computed the coherence with numbers of looks of 9, 25, 49, 81 and 121 (the coherence data of our ERS data was computed from 45 looks). Figure 23 (left) shows the result. The variance in each of the 5 lines is high. If we reduce this by averaging 1000 of such lines, Figure 23 the coherence at the right exceeds 0 in all 5 cases, the difference getting larger for smaller number of looks. Both these features could be expected from Figure 22. A salient detail is the intersection of all curves at (pixel, coherence)=(40.5, 0.4). This is easily explained as follows: the coherence operator (a kind of moving average operator) has no problems to reveal the underlying (high) coherence of 0.8 at the left of the curve. If the operator moves to the right, 0-coherence values enter the computation, which results in an almost linear decrease of the computed coherence. Once enough 0-coherence values are involved, the linear decrease ends, and saturation at a value above 0 sets in (Figure 22 and preceding equation). The linear parts intersect all at the same point.

The above observations led (after several tests on synthetic data) to the following simple edge detection algorithm:

- 1 detect a decrease or increase of 0.3 in the coherence over 2 pixels in the horizontal direction (this is an edge),
- 2 estimate the coherence ρ_{high} of the high side of the edge,
- 3 the edge is at the position for which the coherence is closest to $\rho_{high}/2$,
- 4 repeat steps 1-3 for the vertical direction.

Application to data like that of Figure 23 gave an estimated edge position correct to within (on average) a few tenths of a pixel. The algorithm was then tuned to a tandem ERS image pair (orbit 24917/5244; coherence computation over 15 azimuth pixels times 3 range pixels), and resulted in Figure 24. The edges look rather solid, and the smaller islands are also detected. At the same time the number of false alarms (in the sea) is small

Most commercial image processing packages contain edge enhancement algorithms. We used the Sobel, Prewitt [Gonzalez and Woods, 1993] and (a sort of) difference algorithm from the EASI/PACE package [PCI, 1996]. After enhancement we applied a threshold such that the number of false alarms in the water corresponded roughly to the number produced by our own algorithm (Figure 24). The results are shown in Figure 25 and Figure 26 for comparison with Figure 24.

The Sobel result looks like that of our own algorithm (apart from a difference in printing resolution). The Prewitt result is identical to the Sobel result, apart from a slightly smaller amount of edge pixels in the Sobel result. The difference filter performs worse than the other filters: complete parts of the coast line miss. Whether our algorithm improves upon the Sobel and/or Prewitt filters (especially with respect to edge location precision) can only be concluded from comparison with ground truth data.

4.3 Full resolution lines

The algorithm described in section 4.2 creates an edge map as shown in Figure 24. This figure shows primarily the edge of the island Schiermonnikoog and the coastline of Groningen. The algorithm produces some small features not related to a coastline as well. In this chapter we try to create a coastline using the information of the full resolution image.

The first step is to minimise the features that are not related to a coastline. The false alarms in the edge map are removed using a procedure outlined in [Lee and Jurkevich, 1990]. A buffer is laid surrounding the points marked as an edge by the algorithm developed in section 4.2. This is done to make sure that all the line pieces creating a coastline are connected. Successively the length of each buffered point is calculated. If the buffer is too short the points in the edge map are rejected and are no longer used in the computations. The lines that are long enough are used in the next step of the process.

Within the buffered lines it is possible that a number of points are marked as an edge while only one of them really describes the edge. Therefore the irrelevant points need to be removed. First we fitted a line through the data and calculated the distance from the point towards the line, points that were too far from the line were removed.

At this point in the process the edge map is cleared from extraneous points and the remaining points are represented on a finer grid defined by the full resolution image. The points are represented at the middle of the coarser grid. Combining the information obtained from the edge map with intensity information of the full resolution image using a cost function (see Appendix 2), the ultimate coast line is computed using a smoothing spline fit.

4.4 Test lines

As a test area a part of the island of Schiermonnikoog and its surroundings was chosen. First a coherence map was produced of the test area. Here in range direction 3 cells and in azimuth direction 15 cells were used to compute the coherence between two ERS images. We used the following images: ERS-1 orbit 24917 frame 2529 20-4-96 and ERS-2 orbit 5244 frame 2529 21-4-96. The coherence image produced using these two images is shown in Figure 27. After removing the solitaire edgepoints the edge for our test area looks like Figure 28.

Next the full resolution image from ERS-2 orbit 5244 (21-04-1996) was used to adjust the edgepoints within a certain band to fit the full resolution image. This step is only possible when there is a distinct boundary between land and water visible in the full resolution image. A line was fitted through the edge points detected in the coarser resolution edge image and adjusted on the basis of the full resolution image. The resulting interpolation was performed using a smoothing spline. The result of the procedure is shown in Figure 29. An enlargement of a part of the full resolution edge is shown in Figure 30.

Since this coastline lies in an area where no in-situ data were available several other lines were produced without the adjustment on the basis of the full resolution image. These lines were extracted from the coherence image formed by ERS-1 orbit 24416 frame 2529 16-03-1996 and ERS-2 orbit 4743 frame 2529 17-03-1996 images.

4.5 Conclusion

The full resolution images contain intensity information that is used to improve the spline fit. The fact that the full resolution image improves the coastline is obvious looking at Figure 29. The coastlines obtained from the tandem mission in March oscillate more than the coastlines obtained from the SAR tandem pair in April. Using the eye to inspect the line from April, see Figures 29 and 30, it is shown that this line superimposed on the full resolution image of orbit 5244 frame 2529 agrees with the visible contours between land and water.

5 Coast line validation

The coastlines extracted from the SAR images were compared to the land/water maps that were constructed from the depth maps and the calculated tidal elevations as described in chapter 2. Before this comparison could be done, the coast line had to be transformed from the image co-ordinates in which it is given, to the Dutch National Co-ordinate System, the so-called Rijks Driehoek (RD) co-ordinates in which the land/water maps and the height map are given. This is accomplished by transforming the radar image. Figure 31 shows the original radar image and the transformed image.

The radar image was transformed into RD co-ordinates by selecting ground control points visible in both the radar image and the topographic map. The accuracy of this transformation is about 21 m. The same transformation was applied to the image co-ordinates of the coastline, thus yielding the coastline in RD co-ordinates.

Figure 32 shows the coastline obtained from the April pair plotted over the land/water map. The coastline lies entirely in the no-data area, i.e. the area in which no depths are measured. This coastline therefore can not be compared with the land/water map. The reason for this is the choice of the master image. It was chosen because its baseline is favourable for interferometric applications. Unfortunately, this image was recorded during high tide. When combined with another SAR scene to form a coherence image, only areas that are dry in both scenes can be detected. This implies that the coastline at high tide can be detected from the April pair.

The images of March were recorded during lower tide, see Figure 33, and should be better suited for coast line extraction. Since all images were already co-registered relative to the April image, the coherence between the two March images can be readily calculated, transformed, and overlaid as described before.

Moreover, also the height information of the isle of Schiermonnikoog is available from laser altimetry. Figure 32b shows the coastlines from the April pair (red) and the March pair (yellow) overlaid on the digital map. The blue line is the April coastline shifted to the east (see below). Also the grid points of the tidal model are indicated. Note the overlap between the digital height map and the tidal model. Unfortunately, the coastline extracted from the March pair at lower tide falls outside the range of the digital height map. To analyse the April coastline in more detail, the height of the water column at each tidal model grid point was calculated by subtracting the height of laser altimetry from the water level.

The results are shown in Figure 32c. In the red points the land is dry and at least 15 cm above water level, while in the blue points the water column is at least 15 cm high. In the black points the absolute value of the difference between water level and laser altimeter height is less than 15 cm. This indicates the uncertainty in the results, as the error in the laser altimeter heights is about 15 cm. The coastline should pass through the black points between the red and blue ones. When going from left to right this is indeed the case, but soon the coastline passes through the red points. It seems as if the coastline is too far to the North.

Figure 32d shows the original April coastline in light blue as well as the shifted one in dark blue. The shifted line lies between the red and blue points from the left to point A. At point A the coastline is between the red points. Between points B and C the coastline goes through the black points, and at point D again between the red and blue points. Note that there are blue points north of the black points near point C, indicating flooded areas which can not be found on the topographical maps! This must be due to the coarse grid size of the tidal model or to a poor definition of the coastline on the topographical map. Apparently, the coastline detected from the SAR images is correct.

Figure 34 shows the March coastline overlaid on the land/water map. The coastline of Schiermonnikoog falls between the yellow zone (less than 10 cm above water) and the no-data area. This implies that the coastline as detected from the SAR images is probably right. The coastline of the main land is reproduced well for the dike at the western end, but shows some deviations at the eastern side. This is a land reclamation area, where morphological changes may play a role.

The coastline for the edge of the gully seems to bear little relationship to the land/water map. A possible reason is that the area is flooded twice a day, thus destroying correlation between two SAR scenes. Evidence for this is shown in Figure 35. Though the images show the structure of the sandbanks, this is not reproduced entirely in the coherence image. The two passes are one day apart, and the ripple structure of the sandbank could have changed during flooding. These small morphological changes cause decorrelation, even though both images show the same structure (on a larger scale) in the intensity images. Moreover, not only the sand surface, but also the water distribution on the sandbank could have changed, causing additional decorrelation.

5.1 Prospects of using other SAR sources

The optimum coast line detection method of this report uses two complex ERS C-band images to detect coherence differences, and refines the result with a high resolution intensity image. Some parameters define the performance of a satellite for this purpose:

- 1 Wavelength: the longer the wavelength, the slower the coherence drops with time. So at longer wavelengths land remains coherent for a relatively long time.
- 2 Image resolution: the better the (one look) resolution, the more accurate the coast line estimation.
- 3 Incidence angle: the larger the incidence angle, the smaller the sea backscatter (and the higher the sea-land contrast at moderate wind speeds).
- 4 Polarisation: the sea backscatter is higher for VV than for HH polarisation.
- 5 Signal to noise ratio (SNR): the larger the SNR, the more accurate the coherence.

For our application long wavelength, high resolution, large incidence angles, HH polarisation (if SNR is no problem, VV otherwise), and small SNR are desirable. The following table gives some key parameters of current and future SAR systems. The +-sign in a row indicates the best sensor according to the parameter of that row.

SAR sensor	ERS	Radarsat	ASAR
wavelength [cm]	5.7	5.7	5.7
1 look image resolution [m]	10×5 (+)	8×9	10×5? (+)
incidence angle [deg]	20-26	35-49 (+)	15-45
polarisation	VV (+)	HH	VV and HH (+)
SNR	?	worse than ERS	better than ERS? (+)

According to this table we estimate that ASAR is better than ERS, and ERS better than Radarsat for our application.

5.2 Cost-benefit analysis

5.2.1 Governmental organisations in the Netherlands

Rijkswaterstaat maps the coastline of the North Sea coast every year to assess safety and the need for beach nourishments. These maps are constructed from two kinds of measurements:

- echo sounder depth measurements along transects above sea,
- laser altimeter height measurements on a grid above land.

Both the depth and the height are given relative to NAP. The height measurements are interpolated to predefined transects and attached to the depth measurements. Generally, there is some overlap between the two data sets. The coastline is defined as the contour line at a predefined NAP level corresponding to average high water. This line is compared to a standard line, and if the actual coastline deviates too much from the standard line in the seaward direction, appropriate measures are taken to protect the coast. More information is given by, e.g., [Snijders et al., 1998]. In estuaries like the Waddenzee, coastlines are defined in a similar manner.

The accuracy in the horizontal position of the coastline obtained in this way can be estimated easily. Both laser altimeter and echo sounders have an accuracy between 15 cm and 20 cm. The average beach slope for the coast of Holland is about 0.03 (though slopes in the tidal zone up to 0.2 may occur), leading to a horizontal accuracy of about 7 m. Note that the slope of beaches on the Wadden isles may be much smaller, as low as 0.005, leading to poorly defined coast lines with a horizontal error of 40 m. The shoals in the Waddenzee are flat with bottom slopes as low as 0.0005 and therefore errors in the coast line of 400 m. From an operational point of view, this is not too serious, as these shoals pose no problems. More accurate information would be welcome for the sake of completeness, but only if this information can be obtained easily at low costs.

The costs involved in mapping the coastline are considerable. The laser altimeter measurements cover the beach and the first dunes, a strip of typically 500 m width which must be covered in two passes. The costs for laser altimeter measurements, including processing to a DEM, are about Dfl 4,000.- per km². The soundings are done in transects perpendicular to the coast, extending about 1 km into sea. The separation between the transects is 200 m, which is typical for monitoring. The estimated costs per square kilometer is about Dfl 1,000.- [Briek et al., 1997]. However, it should be noted that these costs depend strongly on the hour rates assumed. Combining the two figures, mapping one kilometre of coastline takes about Dfl 3,000.-, excluding combination of the data sets and additional processing.

A standard radar satellite image covers about 100 km of coastline and costs between Dfl 2,000.- (ERS) to Dfl 5,000.- (RADARSAT). However, these radar sensors have a horizontal resolution of about 25 m which is too poor for extraction of the North Sea coast line. The information is cheap and may be of value in the Waddenzee. A better resolution is offered by airborne radars, but then the costs increase to a level comparable to that of laser altimetry flights, about Dfl 1,000.- per kilometer coast line.

One may conclude that radar methods for coastline extraction are cheaper than the standard methods. It should be noted however that the combination of laser altimetry and echo soundings yields much more information than the coastline alone. This information is also used to check the height of the dunes, important for safety, and the evolution of the sea bottom close to the shore, important for morphological studies.

As stated before, the coastline should be mapped with a horizontal accuracy of 7 m or better. At present, such accuracy can only be met by airborne systems. An along-track interferometric system would be best suited for this, as the time between recordings is short so the land does not suffer from decorrelation due to flooding. Another option is to use a polarimetric system and relate the land/water boundary to the polarisation difference. It is recommended to study this option in more detail, since it may yield a simple method on a pixel-by-pixel basis.

5.2.2 Private sector; application in developing countries

Private sector users carry out activities on a project basis. Coastline information is required for a limited area of interest, which may be located all over the world. Accuracy requirements depend on the phase of the project. In the pre-feasibility and feasibility phase it is important to obtain a good impression of the test site; accuracy of the data is less important. Speed of data delivery is essential, as there is only a limited time to prepare a bid. Remote sensing techniques to determine the location of a coastline may be especially relevant for two phases of a project. In the (pre-) feasibility phase it can provide baseline information on the coastline and whether it is eroding or silting. In developing countries this may be the only source available, especially for historic data (archived images). For sites that are sufficiently close by to make transport of other sensors feasible in practice, remote sensing techniques may still be the only source that can provide the data in time. As there is no real

competition between data sources, the main issue is whether the benefits of using the data (for risk reduction, protection against costly mistakes) outweigh the costs. This depends mainly on the total project costs.

Another phase in which remote sensing techniques can be relevant is after completion of a construction project, if a constructor is obliged to demonstrate that the construction has no adverse effects on the development of the coastline nearby. This requires a location of the coastline during a number of consecutive years. The accuracy requirements of the measurements depend on what variations in the coastline are acceptable. Acquisition of these monitoring data can be planned in advance so that other than remote sensing measurements can be used. However, for these cases the costs of transport may exceed the measuring costs so that determining the coastline from SAR imagery may well be the most cost-effective method.

The ERS satellite SAR images cover a larger area than is usually required for a private sector project and the pixel resolution is at best sufficient. New sensors may improve this situation. For instance Radarsat II, expected to be launched in 2002, will have an ultra-fine mode with a resolution of 3m x 3m and a (sufficient) swath width of 20-25 km. New sensors like this will do much to increase the applicability of remote sensing methods for coastline detection.

References

- J. Briek, J. van Dijke, R. Feron, M. Landsbergen, E. Vaessen and J. Vogelzang, 1997, RWSBAS praktijktesten 1997 (*in Dutch*). Report MS2000+.98.10, RWS-RIKZ. 's Gravenhage, Netherlands.
- G.H. Snijders, Tj. van Heuvel, J.H.M. de Ruig, J. Vreeke, J.W. Theune, W. Visser, A.H. Akkerman, P.J.G. van Elk, B. Dijkstra, P. Noordstra, S. Barsingerhorn, D. Rakhorst, M. Kiezebrink, M. Bubbert, and J. Maranus, 1998, Kustlijnkaarten 1998 (*in Dutch*). Report RIKZ-98.005, RWS-RIKZ, 's Gravenhage, Netherlands.

5.3 Conclusion

The shorelines obtained from SAR images were compared to shorelines obtained by intersecting water level data from model calculations and depth or height data from measurements. The comparison showed that the shorelines obtained from SAR images generally fall within the predicted shorelines. However, the predicted shorelines have a large uncertainty: the error in depth is about 20 cm, the error in height about 15 cm, and the error in water level about 5 cm. Above flat areas like the Waddenzee a decrease or increase of the water level of 10 cm may result in a shift of the shore line of hundreds of meters. This makes it very hard to verify measured shorelines in such areas. The good news is, however, that measured shorelines are a very sensitive measure for morphological changes. Subsidence of the bottom due to, e.g., gas extraction will manifest itself first in a decrease of the area of dry-falling shoals. Moreover, the area of dry-falling shoals itself is an important parameter in the natural value of an area.

Use of repeat-pass interferometric methods for detecting land/water boundaries may be limited in flat, inter-tidal areas, as in this study decorrelation due to flooding has been found even within 24 hours. A two-antenna system with sufficient base line is to be preferred in this respect. Another possibility is to use a polarimetric system and detect land and water from the different intensities at HH and VV. The backscatter of the sea at VV is generally larger than that at HH, while for land the situation is opposite. The polarisation difference may be a good indicator for land and water. To the knowledge of the authors, this has never been studied, and it is highly recommended to do so.

6 Conclusions

Interferometric techniques provide a good way to distinguish land from sea in a SAR image. Straightforward classification based on the coherence yields a visually good result. Inclusion of backscatter intensities in a classification algorithm deteriorates the result.

Although interferometric techniques greatly improves the reliability of land-water boundary detection, there are some drawbacks involved that need to be countered:

- At least two images of the same area are required, which were taken within a period of at most a few months to preserve phase correlation on land.
- The resolution of the obtained coastline is worse (by a factor of about three) than the resolution of the original SLC images.

Several analysis methods of the complex image data were tried to circumvent the need for two images. The method involving azimuth resolution proved to be the only single image method investigated sensitive to land-sea differences. A limitation of the method is the use of a moving window, which smears land-sea boundaries. The method performs most probably worse than interferometric (two image) methods. The method of creating separate images by filtering ERS images in the Doppler frequency domain is on theoretical grounds shown to be of no use for the purpose of land-sea separation

A method was developed to combine the good classification properties of interferometric methods with the high resolution of SLC imagery. The coastline is represented as a spline to enforce smoothness and its position is confined to a low-resolution area, obtained by using edge filters on a classification of the coherence image. Within this low-resolution area the spline coefficients are adjusted using a cost function approach so that the resulting spline boundary smoothly separates high and low intensity areas in the high-resolution SLC image. This improves the coastline estimate, as is obvious from looking at Figure 29 and Figure 34. The coastlines obtained from the tandem mission in March are less smooth than the coastlines obtained from the SAR tandem pair in April. Visually the April shoreline (Figures 29 and 30) superimposed on the full resolution image of orbit 5244 frame 2529 agrees with the visible contours between land and water.

The methods developed in this project yield well-defined high-resolution boundary lines that, we firmly believe, are directly related to the coastline. *A priori* it is not clear whether the found line is the water/sand boundary or the wet/dry sand boundary. In a validation effort the found shorelines were compared to shorelines obtained by intersecting water level and depth data (obtained from measurements and models). The results of this validation showed a general agreement but for the following reasons no definite conclusions could be drawn:

Although images show the structure of sandbanks this does not necessarily mean that the coherence image shows exactly the same structure. Since the two passes are 1 day apart the sandbank has flooded and the ripples could have changed. These small morphological changes of the sandbank between two passes cause the two images to decorrelate even when they show the same structure (on a larger scale) in the intensity images. Moreover, not only the sand surface could have been changed, the water distribution could have been changed as well. Even if the sand structure stays the same, the coherence can change due to a changing water distribution.

The sandbanks are extremely shallow. A 1-cm error in either the water level model results or the elevation measurements can easily result in a shift of tens of meters in the computed coastline. Even errors of 10 cm in validation data set are not unrealistic. This means that the used validation set, the best set with operational data that could be obtained, is not sufficiently accurate to validate the location of the high resolution boundary obtained from SLC SAR imagery.

We believe that coastline detection based on the interferometric coherence is a valid method. In the complicated test area where the new methods were applied the best available operational measurements were not sufficiently accurate to verify or falsify the new methods. For a possible follow-up experiment it is therefore recommended to use a test area with well-defined shoreline, and to perform in situ observations (if possible) of the coastline during the SAR overpasses. On the plus side: we believe the developed method produces a coastline in the test area which is as reliable as the one obtained from laser altimeter measurements, and that series of land-water boundaries can be produced in a more cost-effective way using remote sensing methods.

References

- E.P.W. Attema, "The active microwave instrument on-board the ERS-1 satellite", Proc. of the IEEE, Vol. 79, No. 6, June 1991, pp.791-799
- D. Fernandes, "Simulation of speckled SAR interferogram", Proc. EUSAR 1998, pp.493-496
- J.P. Fitch, "Single antenna interferometer", IEEE Conference on Acoustics, Speech and Signal Processing, Toronto, Canada, May 14-17, 1991
- A.K. Gabriel, R.M. Goldstein, "Crossed orbit interferometry: theory and experimental results from SIR-B", Int. J. Rem. Sens., Vol. 9, No. 5, 1988, pp.857-872
- R.C. Gonzalez and R.E. Woods, "Digital image processing", Addison-Wesley, Reading, MA, 1993, pp.199-200
- P.A. Kelly, H. Derin and K.D. Hartt, "Adaptive segmentation of speckled images using a hierarchical random field model", IEEE Tr. on ASSP, Vol. 36, No. 10, October 1988
- J-S. Lee, I. Jurkevich, "Coastline Detection and Tracing in SAR images", IEEE Trans. Geoscience and Remote Sensing, July 1990, p 662-668
- MAST C-STAR project group, "MAST C-STAR yearly report Feb. 97- Feb. 98", 1998
- C. Oliver and S. Quegan, "Understanding synthetic aperture radar images", Artech House, Norwood, MA, 1998, p.345
- PCI, "Using PCI software", Vol. 1, Ontario, Canada, 1998, pp. 222-224
- W.K. Pratt, "Digital image processing". John Wiley & Sons, New York, 1978
- F.P.Ph. de Vries, "Estimation of the parameters used in the azimuth compression", TNO report FEL-91-B331, November 1991
- H.A. Zebker and J. Villasenor, "Decorrelation in interferometric radar echoes", IEEE TGARS, Vol. 30, No. 5, September 1992, pp.950-959

A web version of this report on World Wide Web:

www.argoss.nl:\ism\index.html

Figures

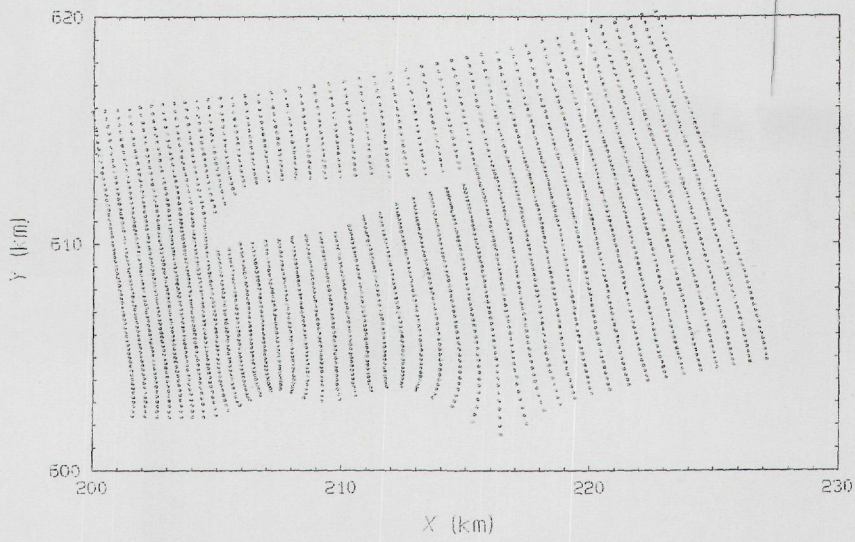


Figure 1 Grid points of the Waddenzee model for the area of interest around Schiermonnikoog (blank area left of the centre). The horizontal co-ordinates X and Y are in km in the RD system.

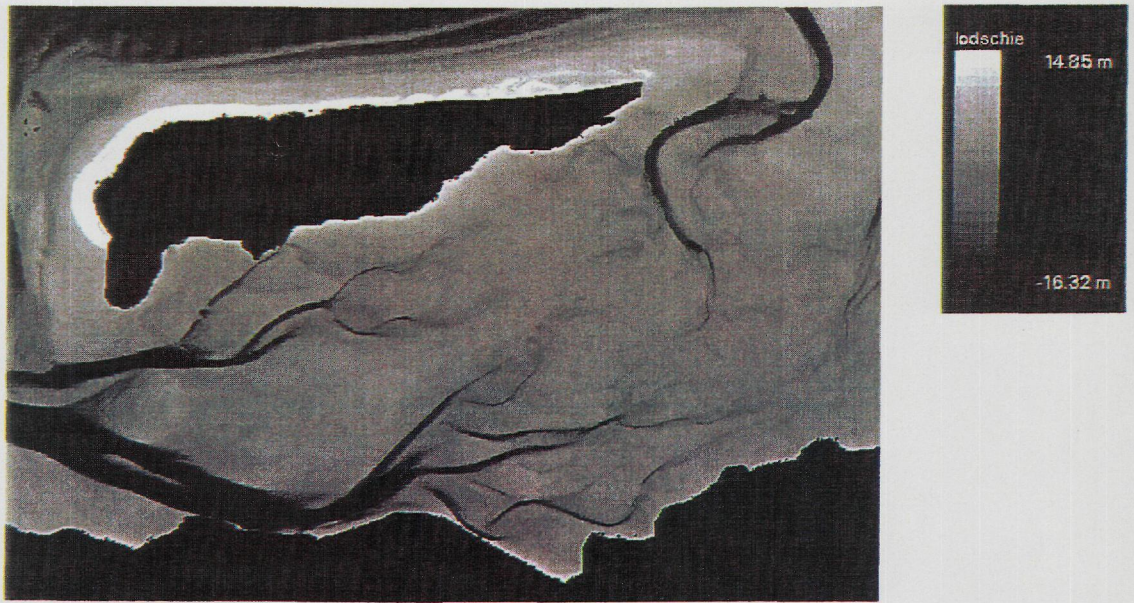


Figure 2a Depth/Height map of the island of Schiermonnikoog and its surroundings.

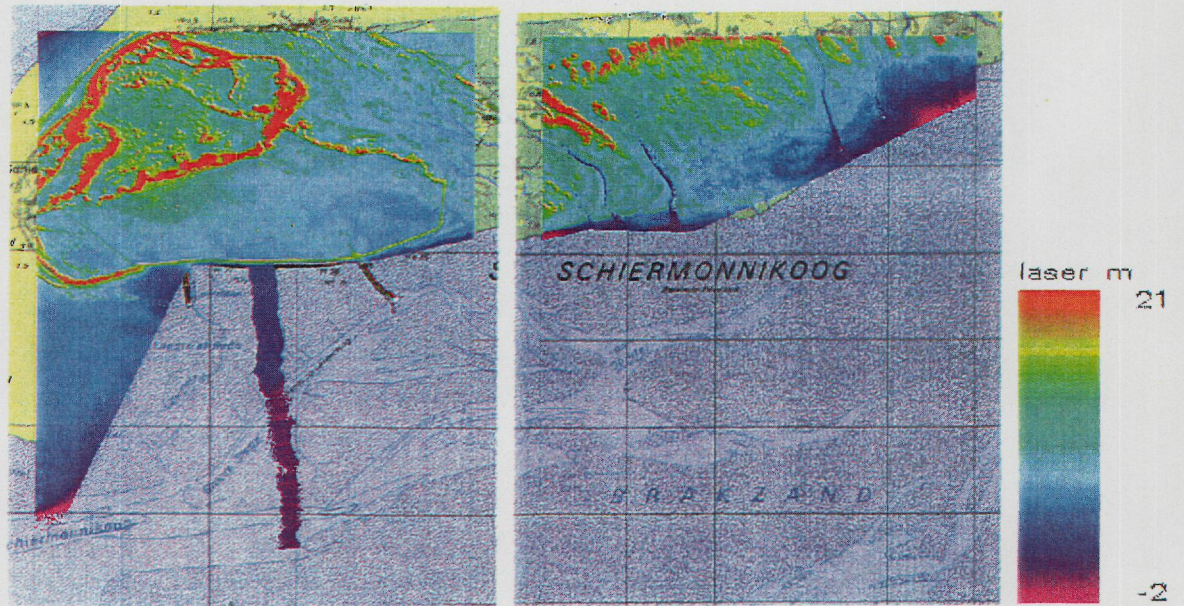


Figure 2b Height map recorded with laser altimetry overlaid on ordinary 1:50000 topographic maps. Note that the two frames are connected, so there is no gap in the height data.

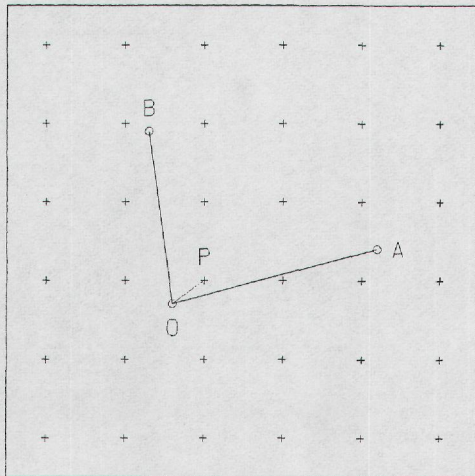


Figure 3 Interpolation of the water level at the coarse Waddenzee model grid (circles) to the fine grid of the depth map (plusses).

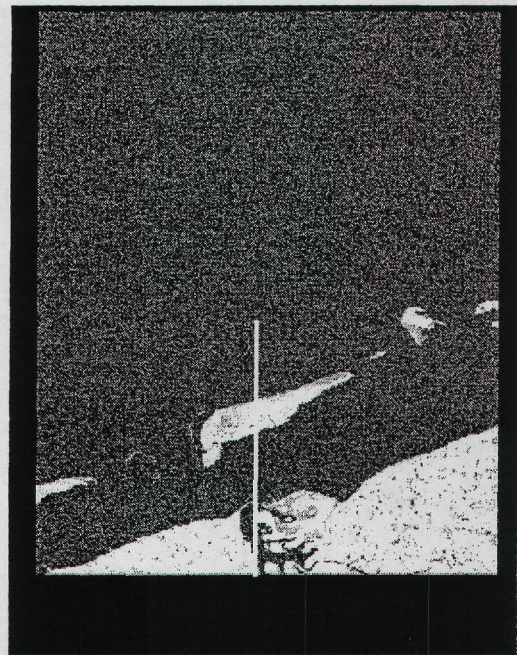
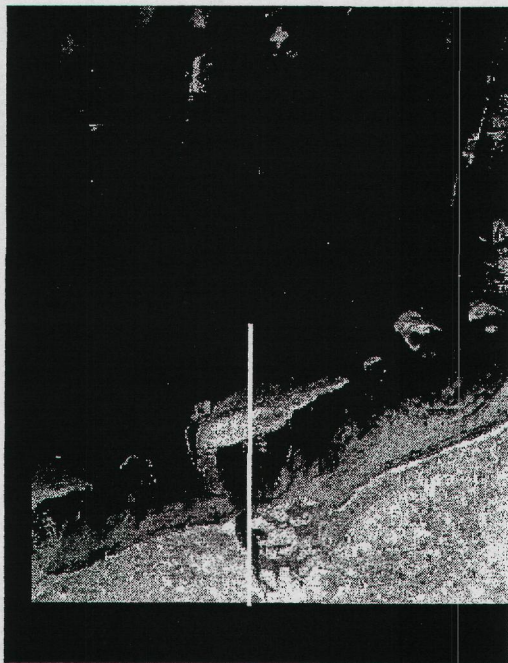


Figure 4 ERS-2 image (intensity) of orbit 5244 (left) and the coherence of the interferogram extracted from a tandem pair of ERS-1/ERS-2 (orbit 24917/5244) images.

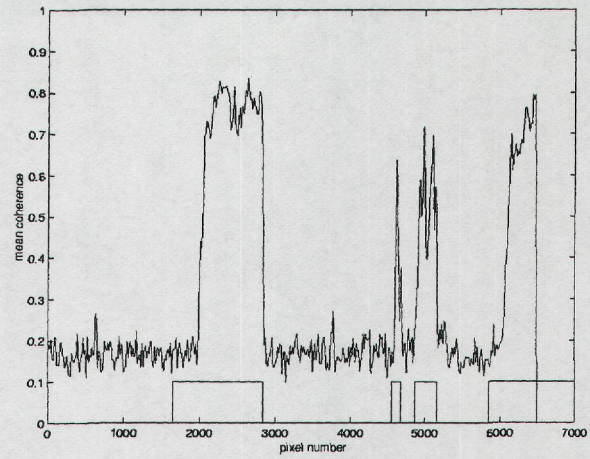
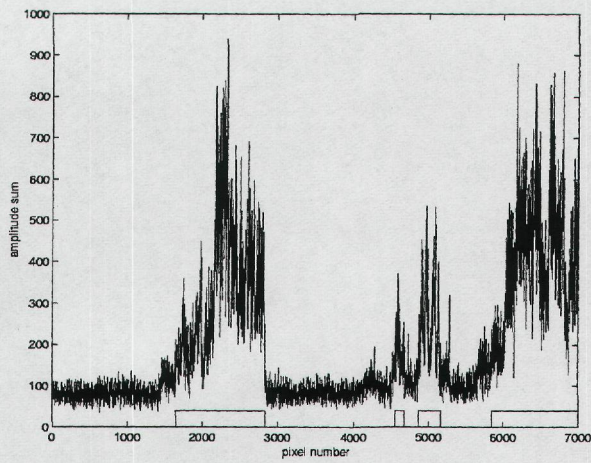


Figure 5 Amplitude sum of ERS-2 data (left) and mean coherence (right).

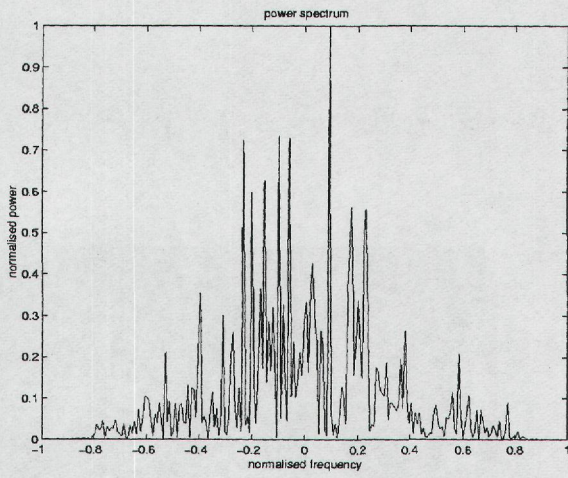


Figure 6 Power spectrum (spectrum centroid ≈ 126.6 if the frequency is 1,2,3,...,256).

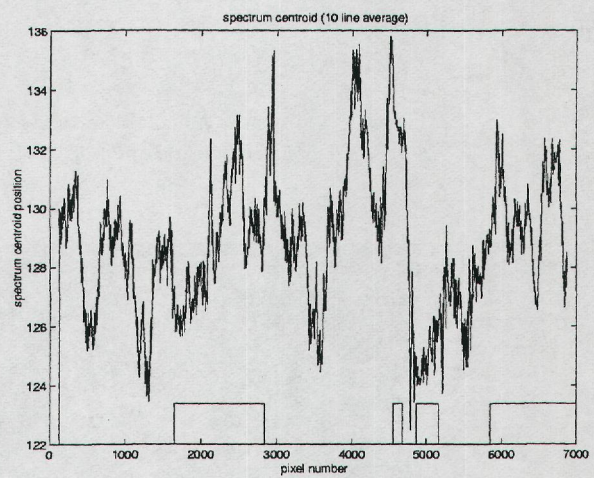


Figure 7 Centroid position

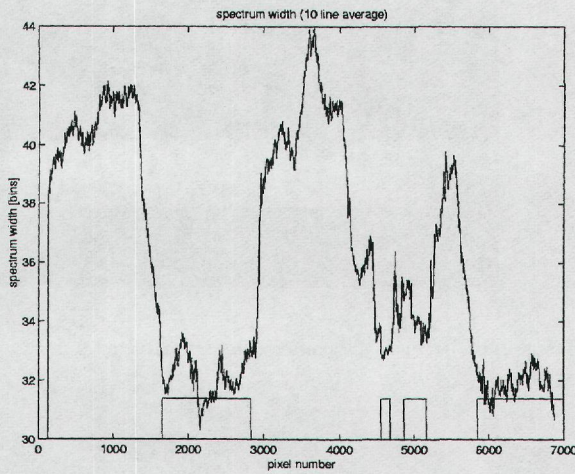


Figure 8 Spectrum widths.

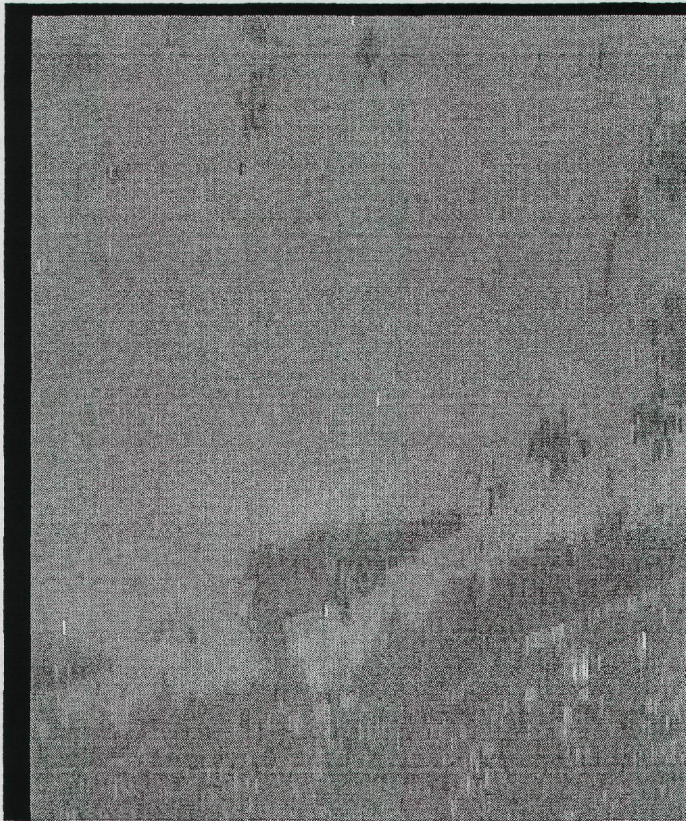


Figure 9 Spectrum width image. Dark areas exhibit a relatively small spectrum width.

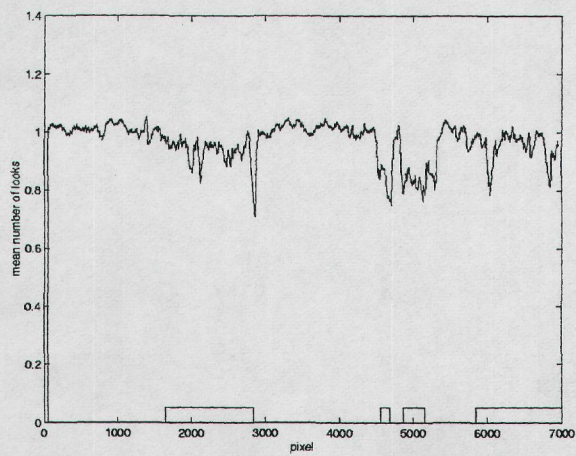


Figure 10 Number of looks, averaged over 10 lines.

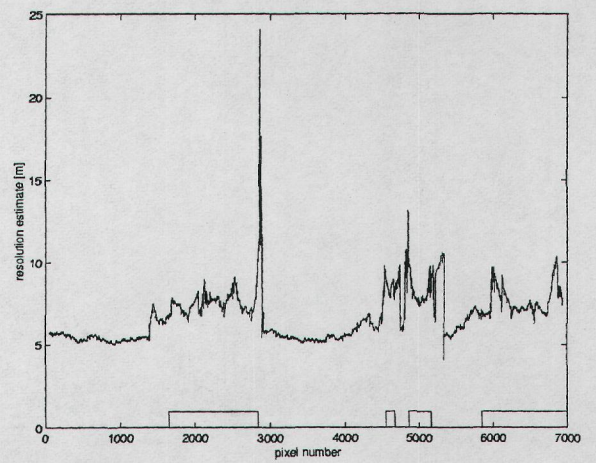


Figure 11 Resolution estimate.

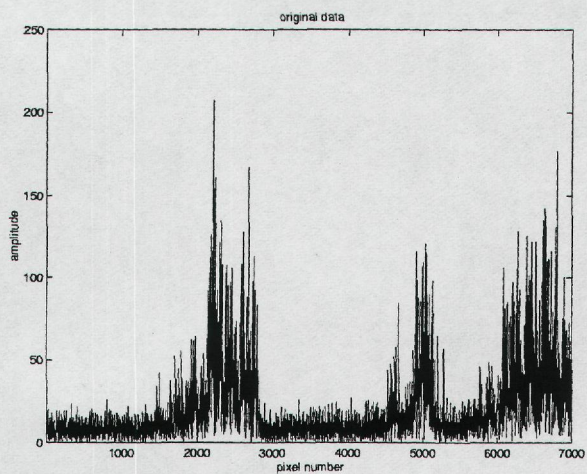


Figure 12 Line of ERS-2 data.

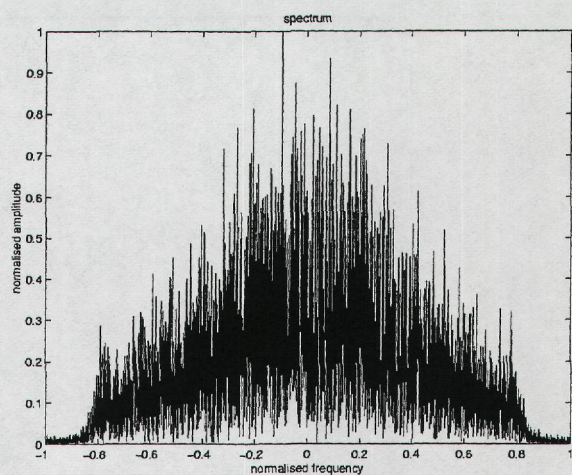


Figure 13 Normalised spectrum of the data of Figure 17.

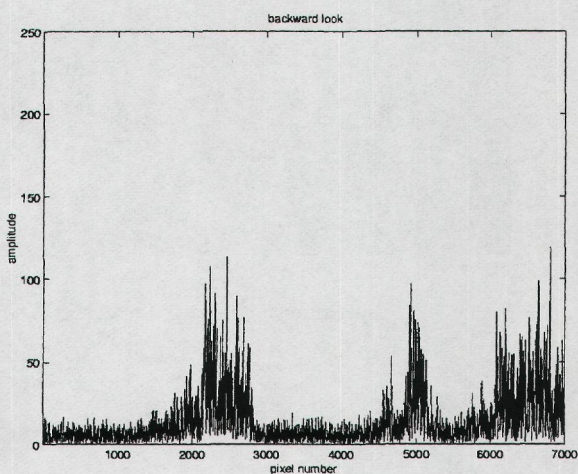
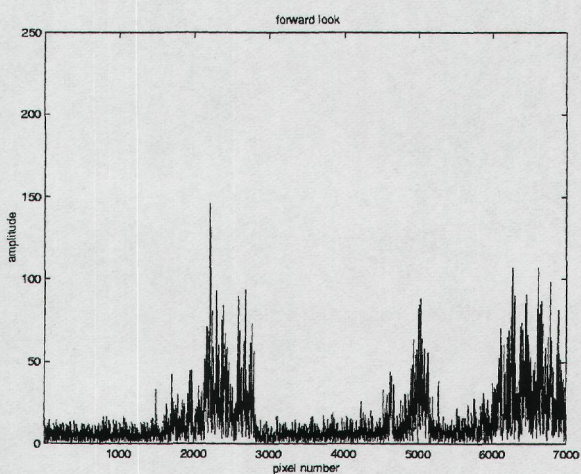


Figure 14 Fore- (left) and aft looks (right).

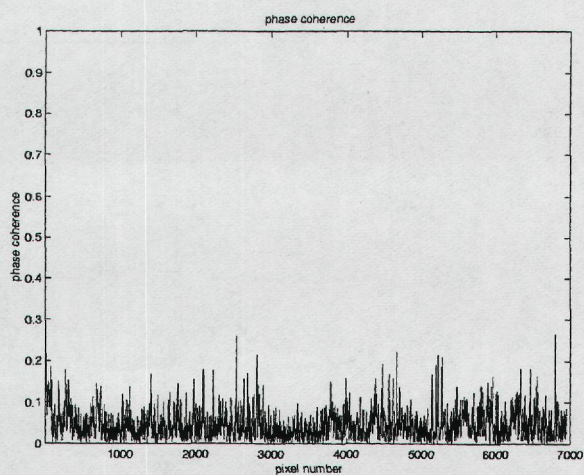


Figure 15 Phase coherence.

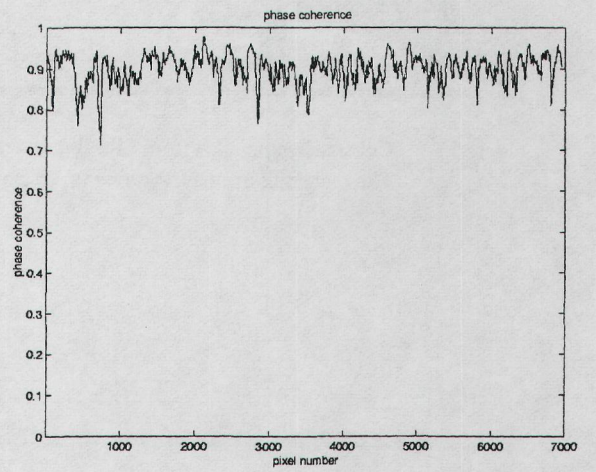
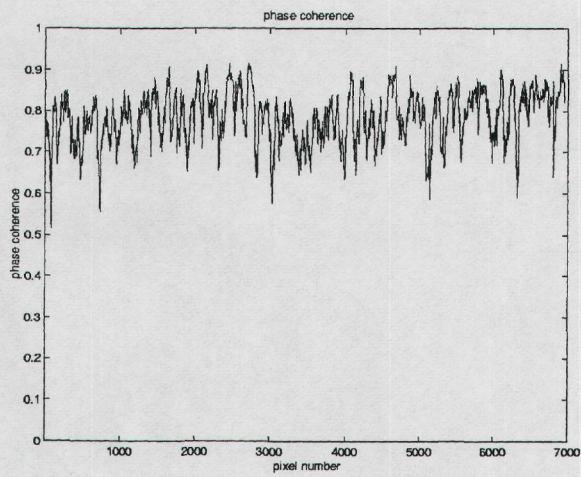
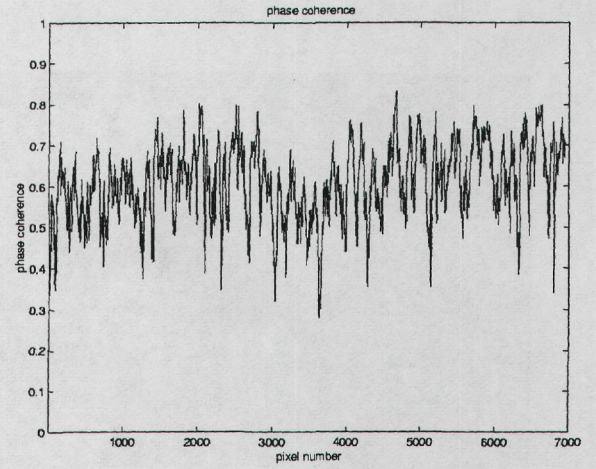
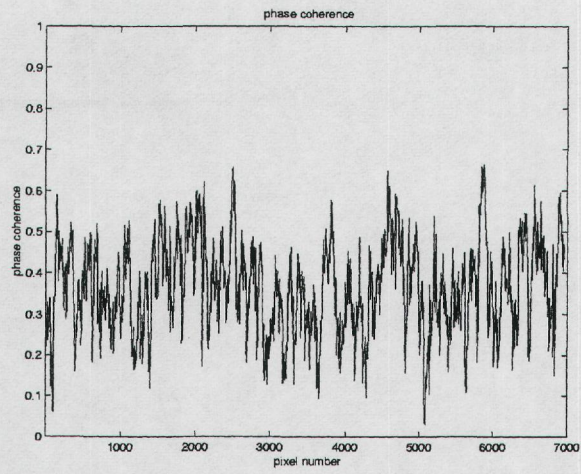


Figure 16 Phase coherence for different overlaps (upper left= 0.2, upper right= 0.4, lower left= 0.6, lower right= 0.8).



Figure 17 Coherence computed from ERS-1/2 images (orbit 24917/5244; see Figure 18).
Time interval: one day. Averaging: 15 azimuth pixels times 3 range pixels.

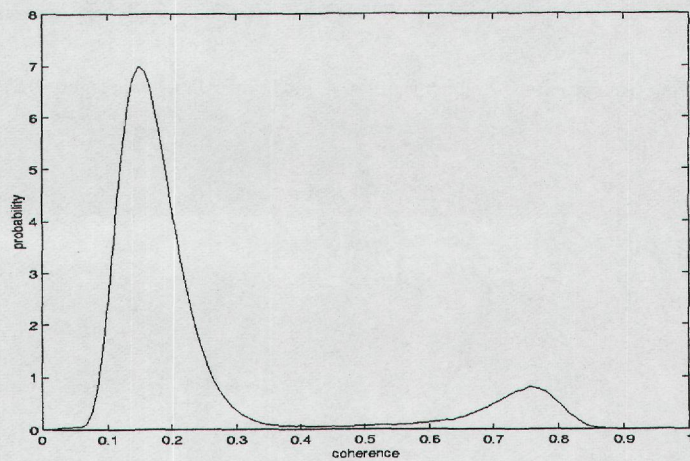


Figure 18 Coherence histogram corresponding to Figure 17.



Figure 19 Classification result of thresholding.



Figure 20 Result of Gaussian MAP classification.

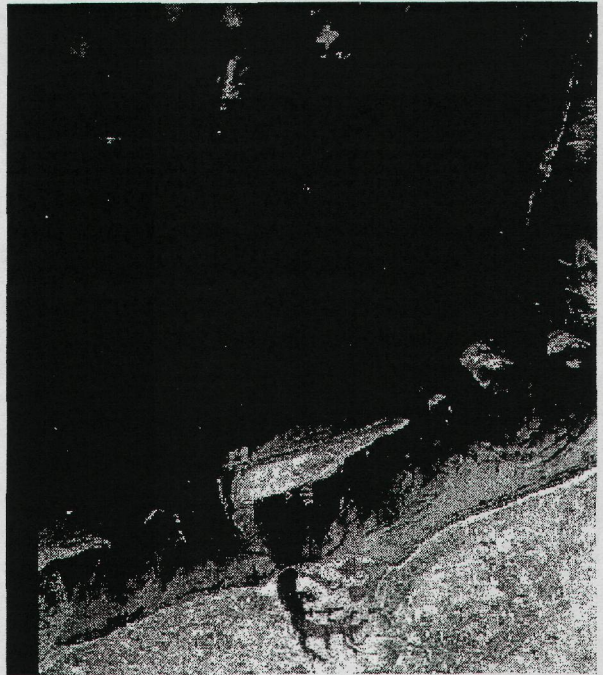


Figure 21 Intensity of ERS-1/2 images (orbit 24917 (left)/5244 (right)).

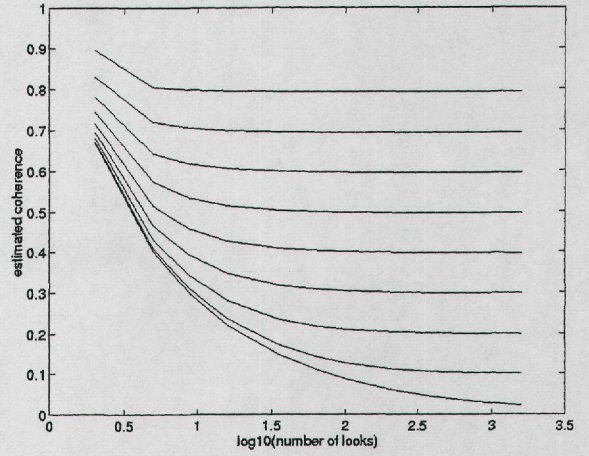
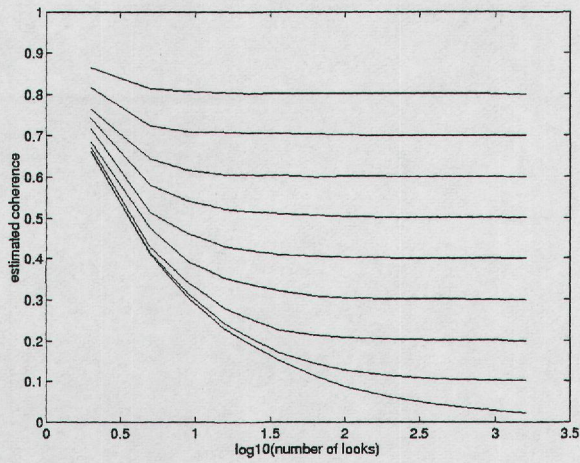


Figure 22 Estimated coherence for simulated data (left) and theoretical result (right). The 'number of looks' is the number of pixels (per image) used in the coherence computation.

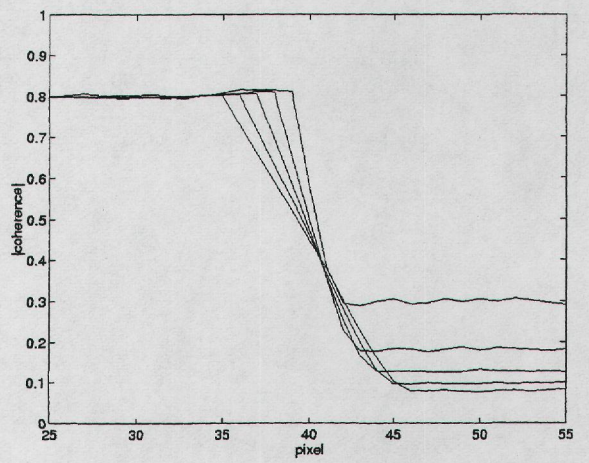
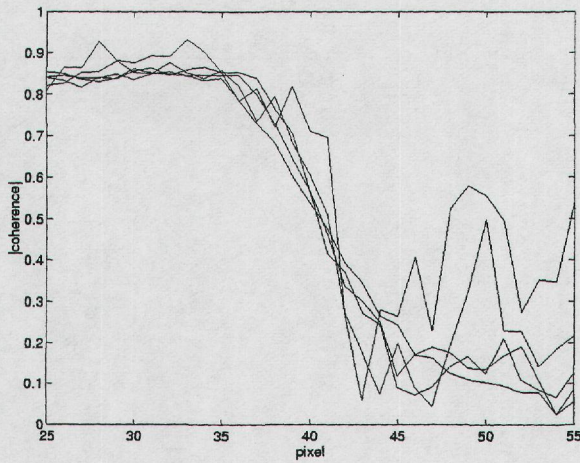


Figure 23 Profile across edge (left: single result; right 1000 results averaged).

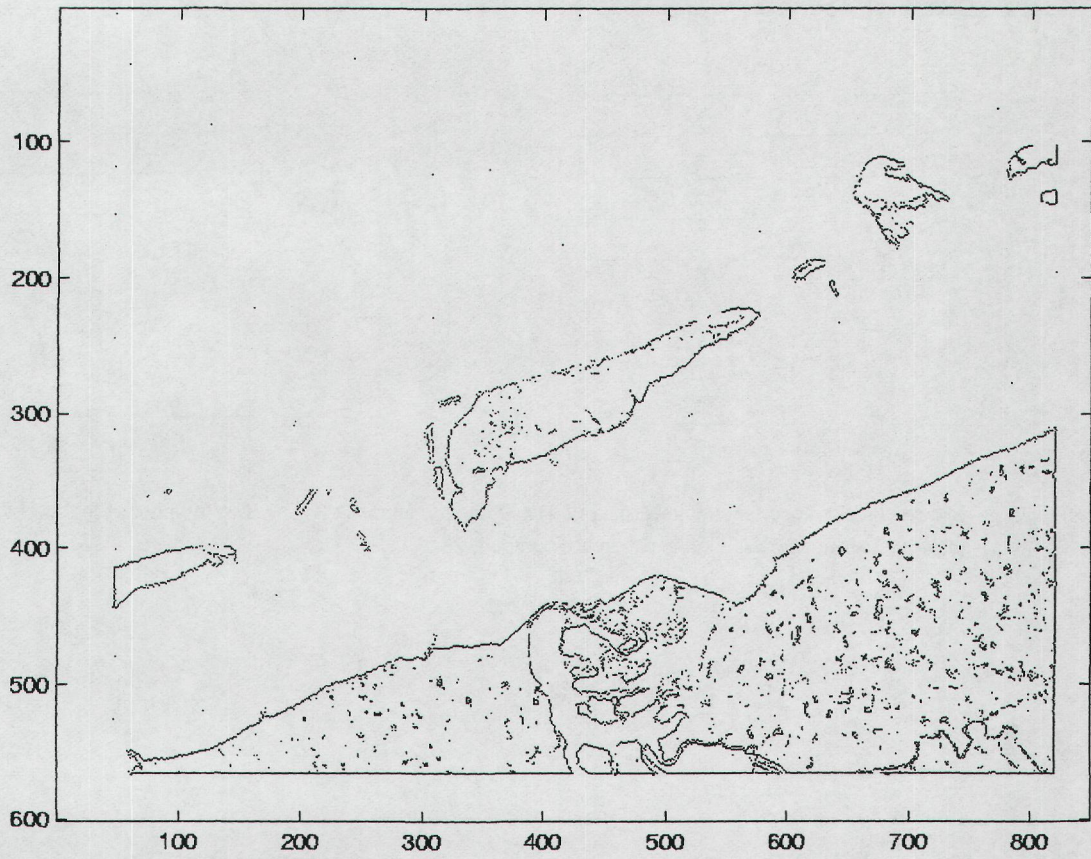


Figure 24 Edge detected image.

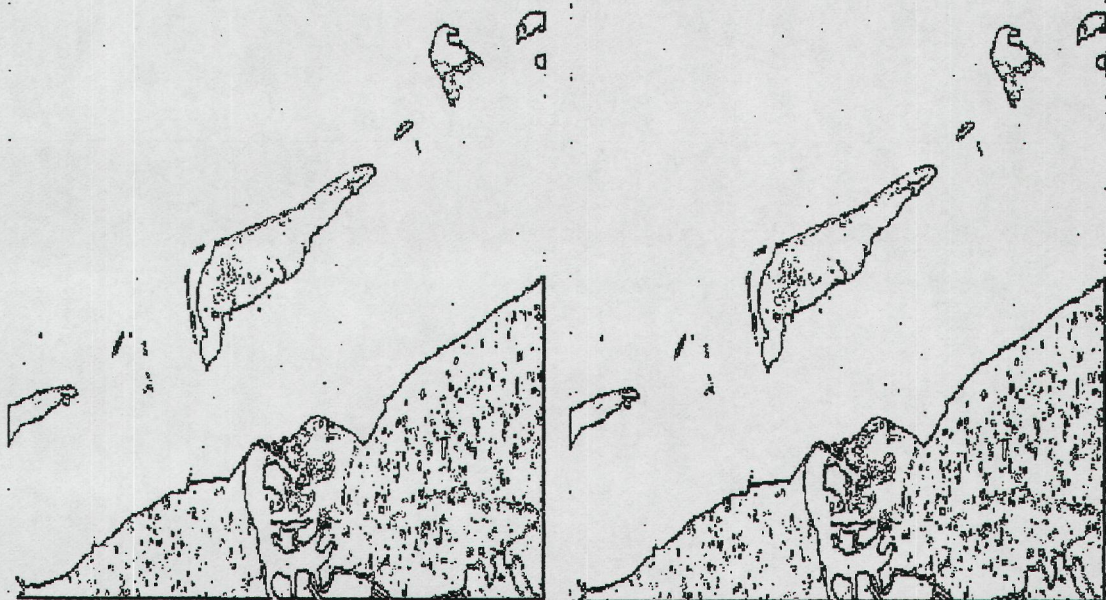


Figure 25 Result of edge detection with the Sobel (left; PCI routine FSOBEL) and Prewitt (right; PCI routine FPRE) operators.



Figure 26 Result of edge detection with a 3x3 differencing edge detection filter (PCI routine FED).

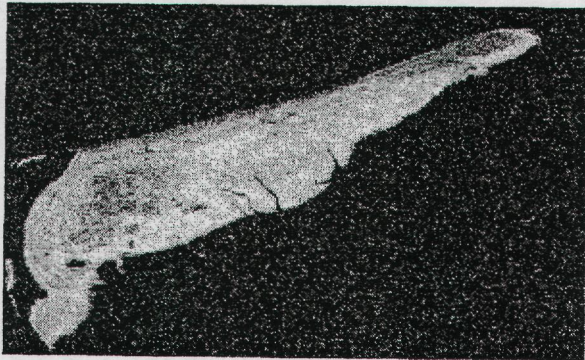


Figure 27 Coherence map of the island of Schiermonnikoog using the tandem pair ERS images of 20-21 April 1996.



Figure 28 Edge map of the island of Schiermonnikoog after removing solitair edge points.



Figure 29 Result of the interpolation.

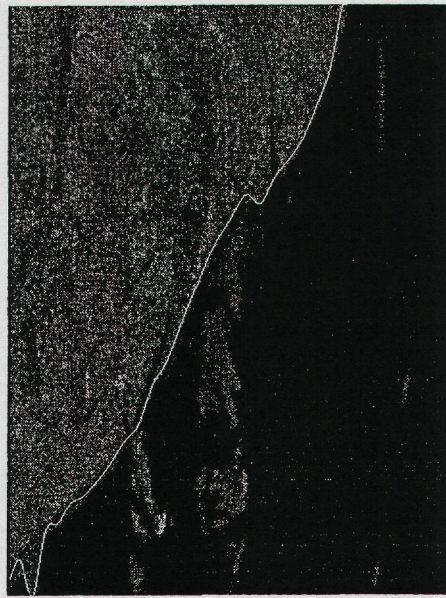


Figure 30 Enlargement of the interpolated edge at full resolution.

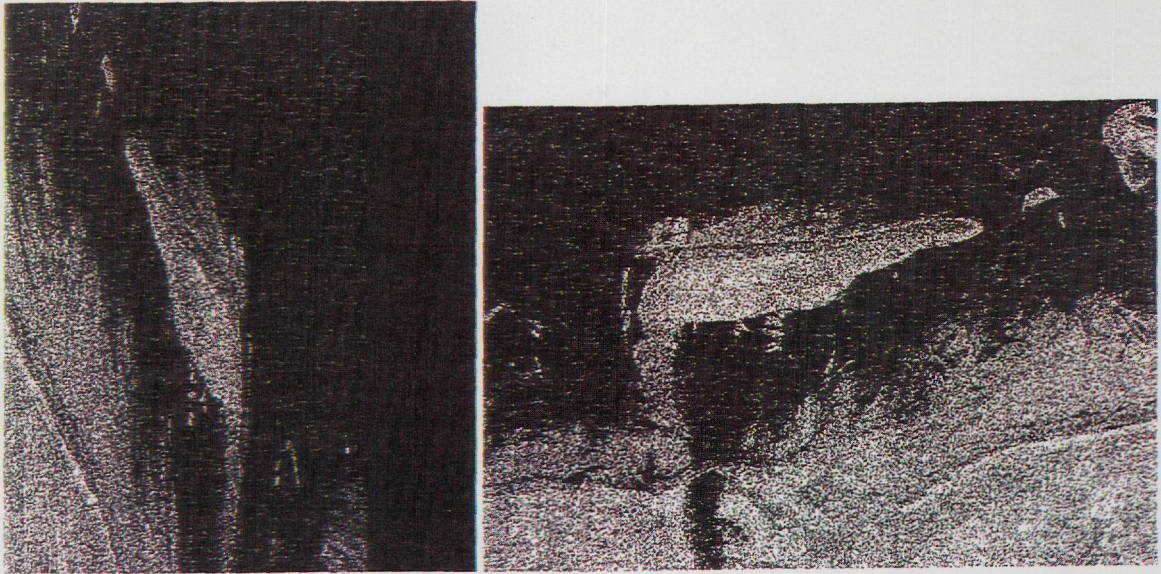


Figure 31 The original master image (left) and the image transformed to RD (right).

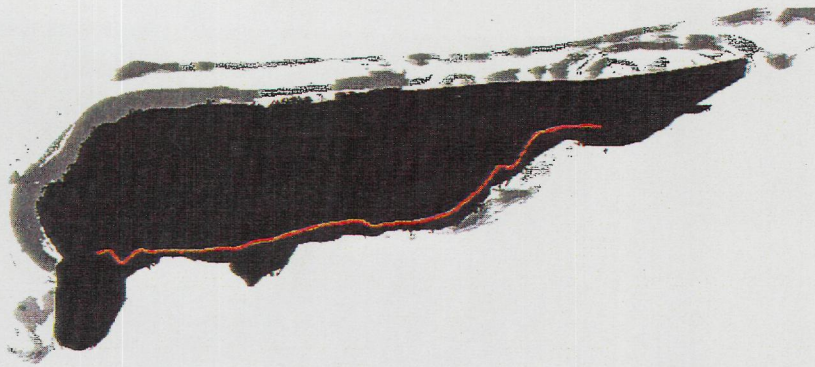


Figure 32a Coast line (red) overlaid on the land/water map. The isle of Schiermonnikoog can be recognised as the black no-data area.

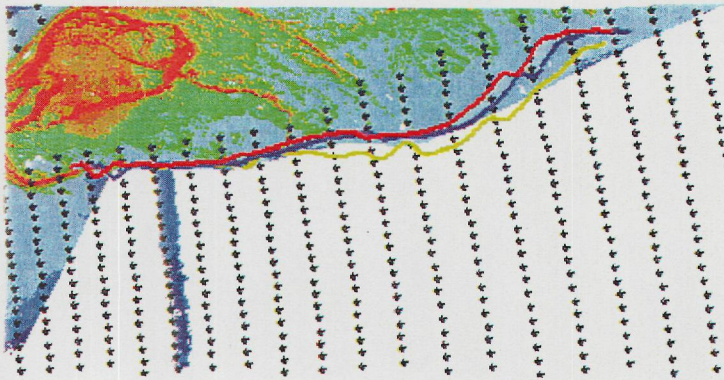


Figure 32b Digital height map and tidal model grid points with the coast lines from the March pair (yellow), the April pair (red) and the shifted April coast line (blue).

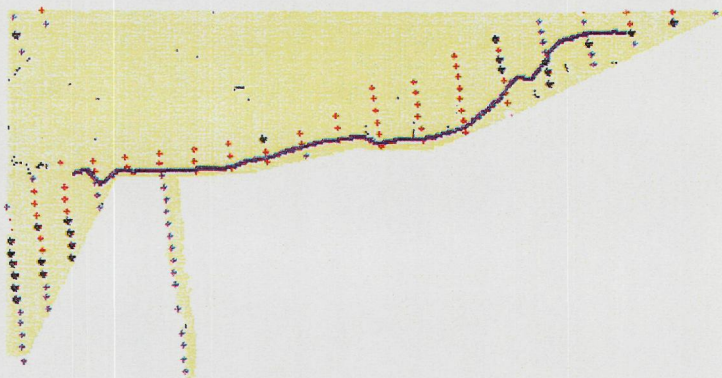


Figure 32c April coastline and tidal model grid points. Points in red are at least 15 cm above water, points in blue at least 15 cm under water. Points in black lie in-between.

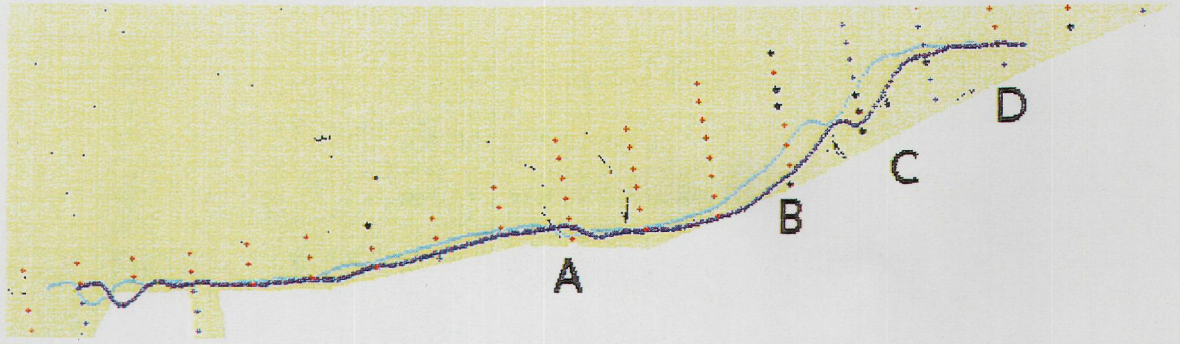


Figure 32d Enlargement of Figure 32c including also the shifted April coastline (dark blue).

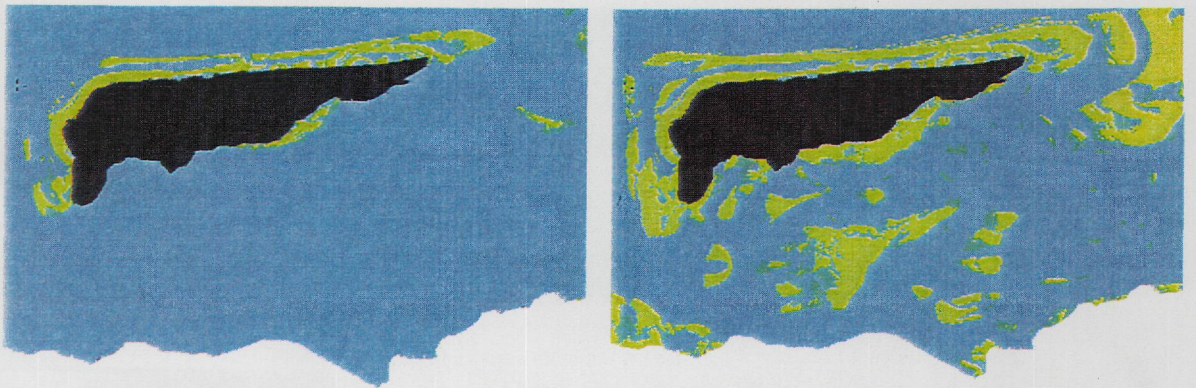


Figure 33 Land/water maps for April (left) and March (right). Blue: at least 10 cm water; green: less than 10 cm water, yellow: less than 10 cm above water, and brown: more than 10 cm above water. Black or white: no data available.

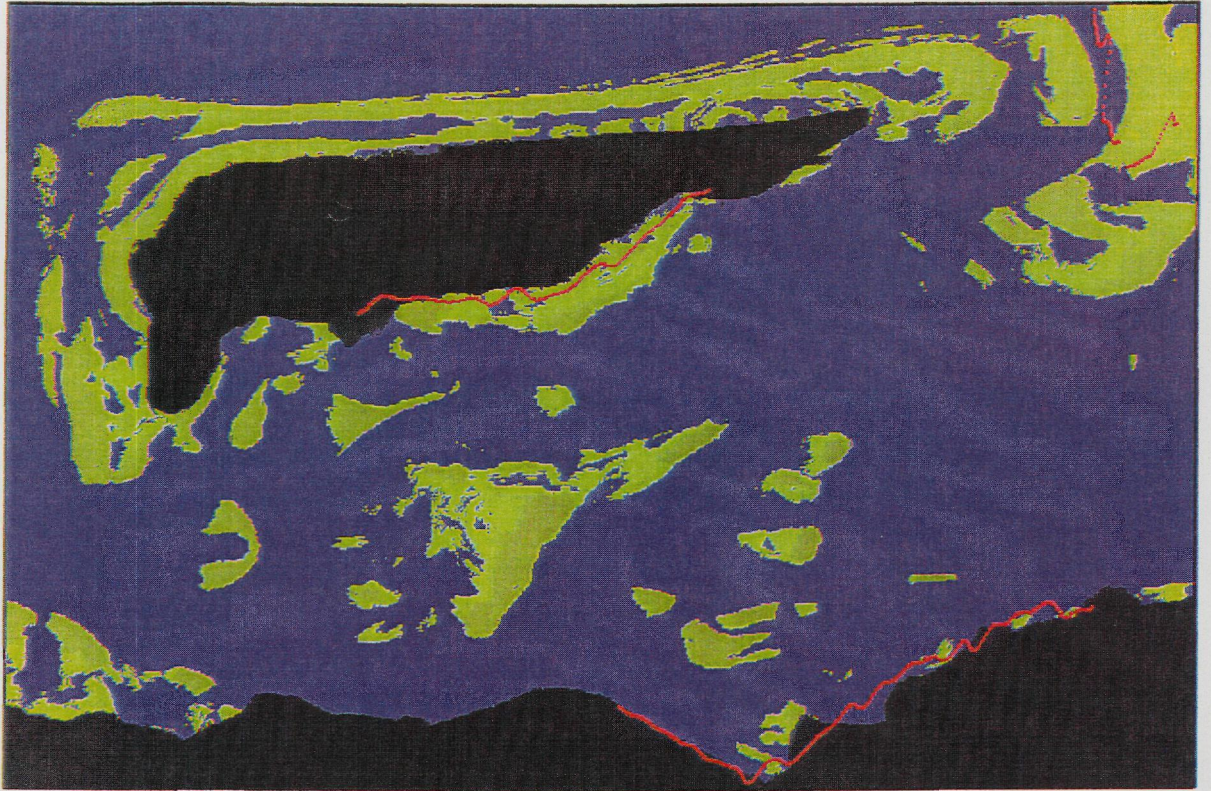
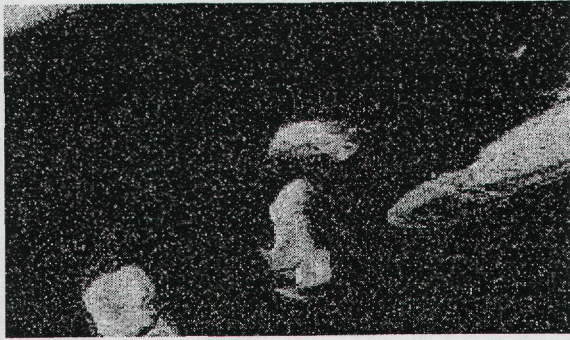
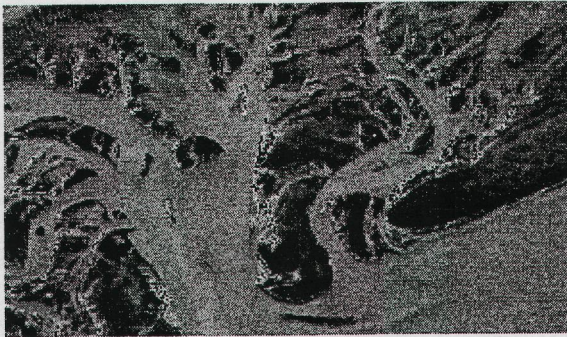


Figure 34 Coast lines in red overlaid on the land/water map for the southern coast of Schiermonnikoog, the coast of the mainland, and the edge of a gully east of Schiermonnikoog (upper right). The no-data areas are indicated by black.



a)



b)



c)

Figure 35 a) The coherence map of ERS1/2 images (orbit 24416/4743 frame 2529) of march,
b) Intensity image of ERS 1 orbit 24416 frame 2529 (16 March 1996)
c) Intensity image of ERS 2 orbit 4743 frame 2529 (17 March 1996)

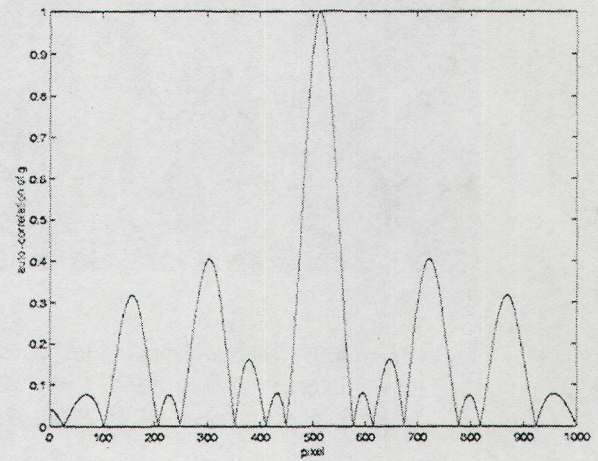
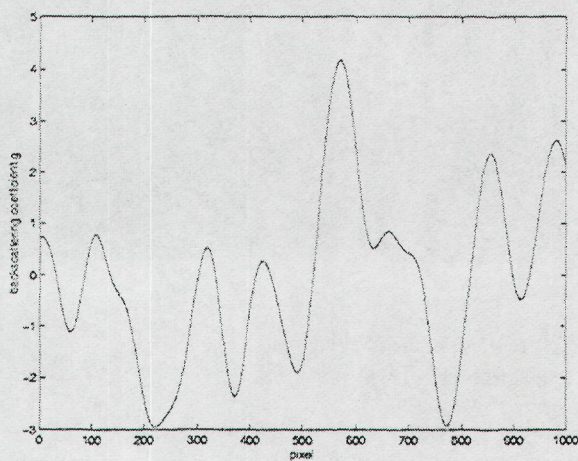
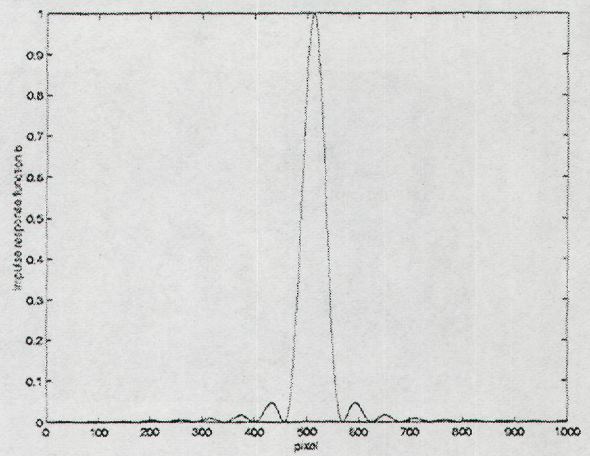
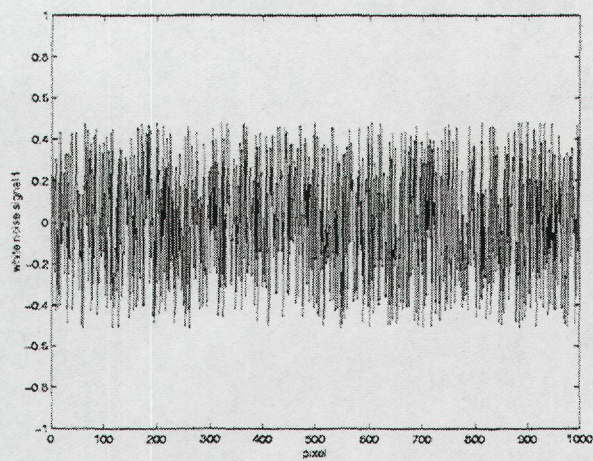


Figure 36 From upper left to lower right: noise f , impulse response function b , backscattering coefficients g and autoconvolution of g .

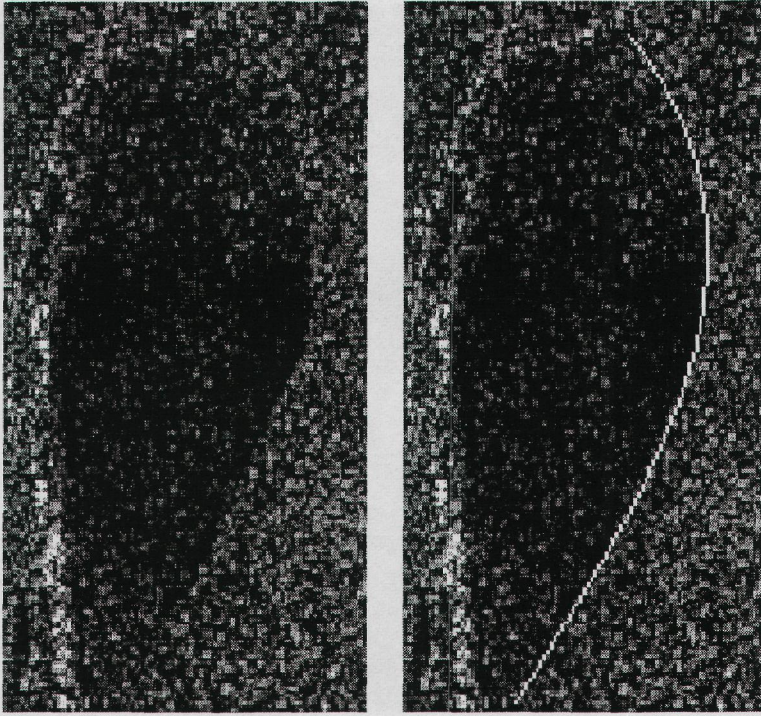


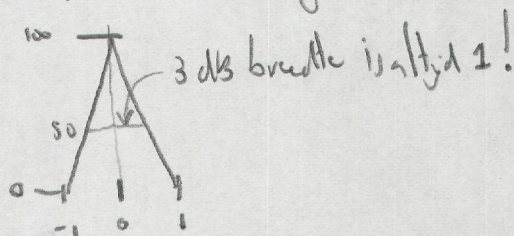
Figure 37 Land-water boundary detection using a cost function

Appendices

(*) N.B. Vast is de data (binnen) kritisch geanalyseerd. Je krijgt dan een hele smalle piek, waarvan de breedte moeilijk te bepalen is.

breedte	andere manier geen interpolatie gebruiken	met interpolatie
0.1	1.5	0.77
1	1.5	0.78
2	3	2.1
5	6	5.0
10	11	10.0
20	21	20.0
50	52	51.0

oortrak: dat is het limietgeval:



(*) Geldt ook (onverant) als je voor $g(x)$ de complexe data neemt, $\sim \sqrt{\sigma^2(x)} \cdot i^y(x)$.
Zou een tabore maat moeten geven dan als je voor $g(x)$ $\sim \sigma(x)$ neemt. (*)

(*) N.B. $f(x)$ is gemiddeld ϕ (ook in simulatie) \Rightarrow toch eigenlijk een complex signaal.

(*) Er blijft dat je voor een e^{-ax^2} impulsbreedte die uit de complexe data bepaalde breedte moet delen door 2. Voor

A1 Spectral resolution estimate (*)

In this appendix we will prove the validity of the resolution estimate

$$\rho_a = \frac{w\left(\left|F^{-1}\left(|F(g)|^2\right)\right|\right)}{\sqrt{2}} \quad (b)$$

First we assume that a line segment of (speckled) backscattering coefficients $g(x)$ (with x the azimuth position [m], and the average of $g(x)$ forced to be 0) is the convolution of a white noise signal $f(x)$ with an impulse response function $b(x)$:

$$g(x) = f(x) \otimes b(x). \quad (c)$$

This implies

$$F(g) = F(f)F(b).$$

$|F(f)|$ is a constant function due to the white noise character of $f(x)$, so

$$\begin{aligned} |F(g)| &\approx |F(b)| \Rightarrow \\ \left|F^{-1}\left(|F(g)|^2\right)\right| &\approx \left|F^{-1}\left(|F(b)|^2\right)\right| \end{aligned}$$

autoconvolute: $F^{-1}(F(f)F(f))$
 autocorrelate: $F^{-1}(F(f)F^*(f))$

f real and even (symmetrisch om $x=0$) \Rightarrow
 $F(f)$ real and even $\Rightarrow F^*(f) = F(f) \Rightarrow$

autoconvolute = autocorrelate

correlation, over \nearrow (assumed to be real and even)

The right hand side of the second expression is the autoconvolution of the impulse response function b . For Gaussian-like functions b the 3 dB width of the autoconvolution is the width of b itself times $\sqrt{2}$ (this is approximately true for similarly peaked functions; for example, for sinc²-like functions this factor is 1.33). Therefore, computing the left hand side of the second expression, determining the 3 dB width of the result and dividing this width by $\sqrt{2}$ gives the resolution estimate ρ_a .

Figure 36 shows an example of the above procedure. We used for the noise f drawings from a uniform distribution [-0.5,0.5]. This implies a zero mean for g . The impulse response function is a sinc² (we thus used the factor 1.33) with a 3 dB width of 50 pixels. The width computed from g with the procedure outlined above is 54 pixels. Repeating this a thousand times gave a mean width of 49 pixels, with 40 % of the widths between 44 and 54 pixels.

The assumption of a white noise signal $f(x)$ is probably more valid over sea than over land: sea exhibits less structure than land. In the latter case $f(x)$ is bandwidth limited. The last equation becomes

$$\left|F^{-1}\left(|F(g)|^2\right)\right| = \left|F^{-1}\left(|F(b)|^2|F(f)|^2\right)\right|.$$

The (spectral) width of $|F(b)|^2|F(f)|^2$ (land) is smaller than that of $|F(b)|^2$ (sea), so the width of the function $|F^{-1}(|F(b)|^2|F(f)|^2)|$ (land) exceeds that of $|F^{-1}(|F(b)|^2)|$ (sea). This implies a larger resolution estimate over land than over sea, the value over sea being closest to the real resolution.

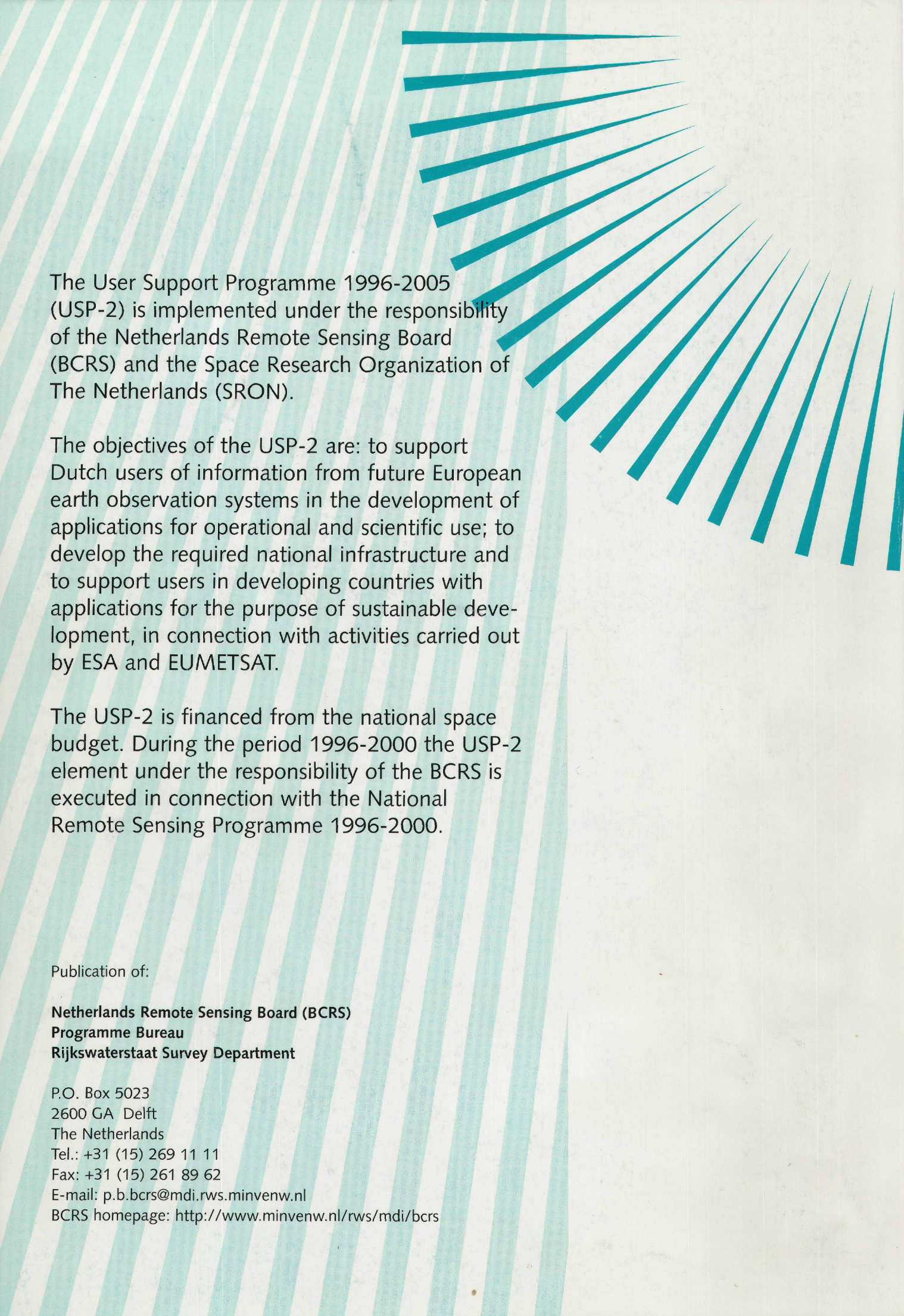
A2 Cost function

A straightforward method is to use a classification scheme and determine the probability that a pixel belongs to the land or the water class:

$$P(x_i) = P_1(x_i)P_2(x_i)\dots P_n(x_i),$$

with x_i the location and P_i the probability density function for the first map made from the SLC image. A problem is that classes need not be characterised by fixed intensities, that the resolution of various maps will differ due to the averaging required by the processing method and that the boundary between the two classes will be ragged due to noise. However, this is a valuable first step to determine where the land masses are located and to give a first guess for the boundaries.

A first guess for a land-water boundary can be further improved with a cost function approach. In this case the boundary is represented as e.g. a spline, thus ensuring smoothness. The spline coefficients are treated as the adjustable parameters in the cost function, which is tuned until the maximum average intensity jump over the boundary is reached. A first example is given below. Part of an SLC image (Figure 37, left) shows dry tide land, having a lower backscatter than the surrounding water. The land-water boundary on the right side is clearly visible by eye. A spline was defined by four knots, fixing the y -points and tune the x -points. The “best” boundary according to the cost function is shown in the right hand side of Figure 37.



The User Support Programme 1996-2005 (USP-2) is implemented under the responsibility of the Netherlands Remote Sensing Board (BCRS) and the Space Research Organization of The Netherlands (SRON).

The objectives of the USP-2 are: to support Dutch users of information from future European earth observation systems in the development of applications for operational and scientific use; to develop the required national infrastructure and to support users in developing countries with applications for the purpose of sustainable development, in connection with activities carried out by ESA and EUMETSAT.

The USP-2 is financed from the national space budget. During the period 1996-2000 the USP-2 element under the responsibility of the BCRS is executed in connection with the National Remote Sensing Programme 1996-2000.

Publication of:

**Netherlands Remote Sensing Board (BCRS)
Programme Bureau
Rijkswaterstaat Survey Department**

P.O. Box 5023
2600 GA Delft
The Netherlands

Tel.: +31 (15) 269 11 11

Fax: +31 (15) 261 89 62

E-mail: p.b.bcrs@mdi.rws.minvenw.nl

BCRS homepage: <http://www.minvenw.nl/rws/mdi/bcrs>